



**Towards a full understanding of the nature of Ni (II)  
species and hydroxyl groups over highly siliceous HZSM-5  
zeolite supported nickel prepared by deposition-  
precipitation approach**

Journal:	<i>Dalton Transactions</i>
Manuscript ID:	DT-ART-02-2014-000399.R1
Article Type:	Paper
Date Submitted by the Author:	26-Jul-2014
Complete List of Authors:	Chen, Bao-Hui; Hunan University, College of Chemistry and Chemical Engineering He, Hao; Hunan University, College of Chemistry and Chemical Engineering Huang, Chen; Hunan University, College of Chemistry and Chemical Engineering Liu, Ya-Juan; Hunan University, College of Chemistry and Chemical Engineering Yi, Wen-Jun; Hunan University, College of Chemistry and Chemical Engineering Wei, Xue-Ling; Hunan University, College of Chemistry and Chemical Engineering An, Jun-Fang; Hunan University, College of Chemistry and Chemical Engineering Chao, Zi-Sheng; Hunan University, College of Chemistry and Chemical Engineering

Towards a full understanding of the nature of Ni (II) species and hydroxyl groups over highly siliceous HZSM-5 zeolite supported nickel catalysts prepared by deposition-precipitation method

*Bao-Hui Chen, Hao He, Chen Huang, Ya-Juan Liu, Wen-Jun Yi, Xue-Ling Wei, Jun-Fang An, Zi-Sheng Chao\**

College of Chemistry and Chemical Engineering, State Key Laboratory of Chemo/Biosensing and Chemometrics, Hunan University, Changsha, 410082, China

\* Corresponding author: *Zi-Sheng Chao*

Tel & Fax: +86-731-88713257;

Email: [zschao@yahoo.com](mailto:zschao@yahoo.com)

## Abstract

Highly siliceous HZSM-5 zeolite supported nickel catalysts prepared by deposition-precipitation (D-P) method were characterized by techniques of Fourier transform infrared (FT-IR), hydrogen temperature programmed reduction (H<sub>2</sub>-TPR), X-ray diffraction (XRD), N<sub>2</sub>-absorption/desorption, field emission scanning electron microscopy (FE-SEM), X-ray photoelectron spectroscopy (XPS), and <sup>27</sup>Al magic-angle nuclear magnetic resonance (MAS NMR). The results showed that the D-P of nickel species occurred predominantly on the internal surface of highly siliceous HZSM-5 zeolite, in which the internal silanol groups located in the hydroxylated mesopores or nanocavities played the key role. During the D-P process, nickel hydroxide was first deposited-precipitated *via* olation/polymerization of neutral hydroxo-aqua nickel species over the HZSM-5 zeolite. With the progress of D-P process, 1:1 nickel phyllosilicate was formed over the HZSM-5 *via* the hetero-condensation/polymerization between charged hydroxo-aqua nickel species and monomer silicic species generated due to the partial dissolution of HZSM-5 framework. The 1:1 nickel phyllosilicate could be also generated *via* the hydrolytic adsorption of hydroxo-aqua nickel species and their subsequent olation condensation. After calcination, the deposited-precipitated nickel hydroxide was decomposed into nickel oxide, while the 1:1 nickel phyllosilicate was transformed into 2:1 nickel phyllosilicate. According to the

above mechanism, Ni(II) species were present in both the forms of nickel oxide and 2:1 nickel phyllosilicate, which were mutually separated each other, being highly dispersed over HZSM-5 zeolite.

**Keywords:** Highly siliceous zeolite; Hydroxyl group; Nickel phyllosilicate; Deposition-precipitation; Mechanism.

## 1. Introduction

Zeolites are microporous crystalline aluminosilicates with well-defined channels and cavities and have been widely used as ion exchangers, molecular sieves, sorbents and catalysts<sup>1-3</sup>. High siliceous zeolites, *e.g.*, ZSM-5<sup>4,5</sup>, mordenite<sup>6</sup>, all-silica ZSM-12<sup>7</sup>, and silicalite-1<sup>8-11</sup> (ZSM-5 with Si/Al ratio up to the infinite limit), are those having a very high Si/Al molar ratio in framework, and display a few advantages relative to their high alumina counterparts. For instances, the large hydrophobicity enables high siliceous zeolites to be very stable in the high pressure, thermal, hydrothermal, and corrosive environments, being very crucial to the applications of these materials<sup>12-14</sup>; the high Si/Al ratio in high siliceous zeolites offers a low concentration of Brønsted acid sites with maybe more strong strength, which is useful to the applications of these materials in acid-catalyzed reactions<sup>15</sup>; the lack or even absence of strong electric fields and gradients in high siliceous zeolites affect probably these material's sorption properties for a number of molecules<sup>16,17</sup>; furthermore, high siliceous zeolites are of theoretical importance in distinguishing which proportion of catalytic behavior of these materials is attributable to high silicon content and which to shape selectivity<sup>18</sup>. Accordingly, high siliceous zeolites have been being paid much attention.

ZSM-5 is a typical representative member of highly siliceous zeolites. It has been broadly utilized as catalyst materials in the commercial catalytic processes

such like catalytic cracking, alkylation and isomerization reactions, due to its unusual shape selectivity, adjustable acidity and other benignities<sup>19-21</sup>. Besides, ZSM-5 zeolite is frequently employed as catalyst support for metal loaded catalyst, owing to its high specific surface area, enhanced metal-support interaction<sup>22</sup>, and large feasibility in forming bifunctional catalyst<sup>23</sup>. Both of the applications of ZSM-5 as catalyst and catalyst support are related very deeply to the structural hydroxyl groups contained in this zeolite. It is known that ZSM-5 contains not only bridging hydroxyl groups (Si(OH)Al) as Brönsted acid centers but also abundant silanol (Si-OH) groups. For example, within a HZSM-5 zeolite, up to 8 % of the lattice Si atoms are present as silanol groups<sup>24</sup>. The silanol groups consist of terminal silanol groups (external Si-OH) situated on the external surface and intracrystalline silanol groups (internal Si-OH) located at various structural defects of ZSM-5 zeolite. A cluster of four internal SiOH groups in the vicinity to each other, caused due to the T atom missing, is known as "hydroxyl nest"<sup>4, 8, 25</sup> and the aggregation of "hydroxyl nests" forms hydroxylated nanocavities. These internal Si-OH groups have been found to play versatile roles, *e.g.*, behaving as the catalytically active centers<sup>26</sup>, allowing for the grafting of heteroatoms<sup>4</sup>, providing the strained and reactive Si-O-Si bridges<sup>8</sup>, and even enhancing the molecular mobility of guest molecules within the defective structure<sup>24</sup>.

Metal modified zeolites are among the catalysts being of most industrial importance. A few methods have been developed to prepare the metal modified zeolite catalysts. The methods of metal ion-exchange<sup>27</sup>, isomorphous substitution of T atoms by metal atoms after<sup>28</sup> or post<sup>29</sup> synthesis were usually employed to prepare the catalyst with high dispersion of metal component. However, these methods are largely limited by the low loading of metal component<sup>30</sup>, *e.g.*, only an exchange capacity *ca.* 3 ~ 7 mequiv/g in zeolite was achieved by utilizing ion-exchange method<sup>30</sup>. By employing the impregnation and precipitation methods, the catalyst with a high loading of metal component could be obtained<sup>29</sup>, but these methods are restricted to the low dispersion of metal component. To overcome the above issues, Geus *et al.*<sup>31</sup> developed a deposition-precipitation (D-P) method for the preparation of supported nickel catalyst. It involved the first dispersion of silica as support in a solution of nickel nitrate and precipitator urea at room temperature and subsequently the gradual hydrolysis of urea at controlled temperature to generate homogeneously hydroxide ions in the whole solution, depositing the nickel species onto the support. The advantage of this method is that the precipitation of nickel hydroxide in solution phase, due to local supersaturation, can be effectively avoided, enabling all the nickel ions to be homogeneously deposited only onto the support under the interaction between the nickel species and support. Employing the D-P method, the catalysts with a high dispersion and

considerably large loading (> 20 wt.%) of nickel over various supports had been prepared, e.g., Ni/SiO<sub>2</sub><sup>31-33</sup>, Ni/H $\beta$ -Zeolite<sup>29</sup>, Ni/SBA-15<sup>34</sup>, and Ni/MCM-41<sup>35</sup>. In fact, the D-P method was already applied in the preparation of commercially standard Ni/silica catalyst, *i.e.*, EuroNi-1<sup>36</sup>. Nevertheless, it was reported that the properties of catalysts prepared by the D-P method, such as, morphology, dispersion, loading and surface phases composition of Ni(II) species, were obviously affected by the surface area of support and D-P time<sup>29, 31, 35</sup>. The D-P process could be controlled by the dynamic and/or thermodynamic factors<sup>29, 31-33</sup>, and two competition reactions<sup>33</sup>, *i.e.*, Ni-O-Si heterocondensation / polymerization and Ni-OH-Ni olation / polymerization, might be present, which were responsible to the generation of nickel phyllosilicates and nickel hydroxides, respectively, on the support.

As has been known, the metal/support interface, being of considerably large importance in heterogeneous catalysis, is related closely to the dispersion, reductivity and anti-sintering property of metal over support, and accordingly, the performance of supported metal catalyst<sup>37</sup>. While a few studies on the interface between metal and oxide (*e.g.*, alumina, silica, etc.) were documented in the literature<sup>38-40</sup>, the metal/zeolite interface has been less investigated. In our previous work<sup>5</sup>, highly siliceous HZSM-5 supported Ni catalysts were prepared by the D-P method, and those catalysts had been found to exhibit excellent catalytic activities

for the synthesis of catechol *via* the dehydro-aromatization of 1, 2-cyclohexanediol. This paper dealt with mainly the identification of surface composition, structure, and morphology of highly siliceous HZSM-5 supported Ni catalysts prepared by D-P method. It was aimed to clarify the natures and changes of Ni (II) species and hydroxyl groups over the interfaces of Ni/high siliceous HZSM-5 zeolite during the D-P process. The results obtained were expected to provide a molecular-level interpretation on the generation of highly-dispersed supported metal catalyst prepared by D-P method.

## 2. Experimental section

### 2.1 Preparation of catalysts

HZSM-5 zeolite (purchased from Fuxu Zeolite Corporation, China) with a molar ratio of Si/Al =100 was first calcined in air at 550 °C for 4 h and then employed as the support in the subsequent preparation of HZSM-5 supported Ni catalysts.

HZSM-5 supported Ni catalysts were prepared by the deposition-precipitation (D-P) method. HZSM-5 was first dispersed into a 7.5 wt. % aqueous solution of urea (analytical purity), with a liquid/solid weight ratio of 50, at room temperature

and under stirring. Then, according to a 20 wt. % of theoretical loading of Ni in catalyst, a calculated amount of 2.5 wt. % aqueous solution of nickel nitrate (analytical purity), was added, and the resultant mixture was heated to 95 °C in 20 minutes under stirring. After stirring and heating at that temperature for a chosen time (1 ~ 24 h), namely D-P time, the precipitates were recovered by separation, washing with de-ionized water and drying at 80 °C for 12 h. The resultant powders were calcined in air at 450 °C for 4 h, generating the HZSM-5 supported Ni catalysts, namely Ni/HZSM-5(X), where X refers to the D-P time expressed in hours (1 ~ 24 h). For example, Ni/HZSM-5(2) represented the catalyst that was prepared *via* 2 hours of D-P. To figure out the effect of calcination, the catalysts prepared *via* the above procedure but without the step of calcination at 450 °C were also employed in the studies, and these catalysts were specially denoted as uncalcined Ni/HZSM-5(X).

As had been reported, the Ni loading depended largely on the D-P time<sup>33</sup>, and thus, after the D-P procedure, the actual loading of Ni, namely  $Ni_A$ , could be lower than the theoretical loading of Ni, namely  $Ni_T$ . In this work, the  $Ni_T$  over all the catalysts, as pointed above, had a value of 20 wt. %, and the  $Ni_A$  were determined by atomic absorption spectroscopy (AAS; see section 2.2). The difference between the  $Ni_T$  and  $Ni_A$  was evaluated by the yield of Ni loading ( $Y_{Ni}$ ), which referred also

to the recovery rate of Ni after the D-P procedure. The calculations of  $Ni_T$ ,  $Ni_A$  and  $Y_{Ni}$  were expressed as follows:

$$Ni_T \text{ (wt. \%)} = 20 \text{ wt. \%} = \frac{W_{Ni,T}}{W_{Ni,T} + W_{HZSM-5,T}} \times 100\%$$

$$Ni_A \text{ (wt. \%)} = \frac{W_{Ni,A}}{W_{catalyst}} \times 100\%$$

$$Y_{Ni} \text{ (wt. \%)} = \frac{Ni_A}{Ni_T} \times 100\%$$

, where  $W_{Ni,T}$  and  $W_{HZSM-5,T}$  referred, respectively, to the weight of Ni in the aqueous solution of nickel nitrate and that of HZSM-5 used for the preparation of catalyst;  $W_{Ni,A}$  represented the actual weight of Ni in the catalyst, determined by AAS;  $W_{catalyst}$  stood for the weight of catalyst used in the AAS determination.

## 2.2 Characterization techniques

Fourier transform infrared (FT-IR) spectroscopy was carried out over a Varian 3100 spectrometer. The specimen was first mixed and ground thoroughly with KBr, followed by pressing into a small circular disc with a diameter of 1 cm, and then employed in the conventional, vacuum or pyridine-adsorption IR determinations. All the determinations were conducted in a transmission mode, and each spectrum was recorded as a result of the accumulation of 32 scans taken at a resolution of 2

$\text{cm}^{-1}$ . The  $1882 \text{ cm}^{-1}$  band for the Si-O overtone of zeolite framework was used as internal standard to normalize the absorbance values<sup>6</sup>. In the conventional FT-IR experiment, the specimen was mounted in a standard transmission sample holder exposed to atmosphere, and the spectrum was collected using the DTGS detector. In both the vacuum FT-IR<sup>41, 42</sup> and pyridine-adsorption FT-IR experiments, the specimen was mounted in an all-quartz IR cell connected to a high vacuum manifold, which was allowed for various *in situ* procedures, *e.g.*, heating, degassing and charging desired gas, and the spectrum was recorded using a MCT detector cooled by liquid nitrogen. For the vacuum FT-IR experiment, the specimen was pre-vacuumed for 8 h under  $10^{-5}$  Torr at a certain temperature, followed by cooling to room temperature, and then, the IR spectrum was recorded. For the pyridine-adsorption IR experiment, the specimen was first pretreated as above for the vacuum IR experiment, and then, exposed to pyridine vapor at room temperature for 1.5 h. After that, the specimen was heated at  $250 \text{ }^{\circ}\text{C}$  for 1 h to desorb the physically adsorbed pyridine in a flow of  $\text{N}_2$ , followed by vacuuming under  $10^{-5}$  Torr at room temperature for 3 h, and then, the IR spectrum was recorded.

Diffuse reflectance ultraviolet visible spectroscopy (DRS UV-Vis) was conducted using a Perkin Elmer Lambda 35 spectrometer, equipped with a 60 mm integrating sphere, using  $\text{BaSO}_4$  as standard.

Temperature programmed reduction of hydrogen ( $H_2$ -TPR), temperature programmed desorption of hydrogen ( $H_2$ -TPD) and temperature programmed oxidation of oxygen ( $O_2$ -TPO) experiments were all performed over a Quantachrome Autosorb-1 instrument equipped with a TCD analyzer, employing a quartz reactor. In the  $H_2$ -TPR experiment, the specimen (50 mg) was first heated to 400 °C at a rate of 10 °C·min<sup>-1</sup> in a flow of  $N_2$  (40 ml·min<sup>-1</sup>). After pretreating under the above condition, the specimen was cooled to 50 °C and exposed to a flow of 10 %  $H_2$ /Ar (40 ml·min<sup>-1</sup>). Then, the temperature was increased from 100 °C to 800 °C at a rate of 15 °C·min<sup>-1</sup>, maintaining the  $H_2$ /Ar flow, and the signal of  $H_2$  as a function of temperature was recorded. In the  $H_2$ -TPD experiment, the specimen (300 mg) was first heated from room temperature to 500 °C at a rate of 10 °C·min<sup>-1</sup> in an atmosphere of flowing 10 %  $H_2$ /Ar (30 ml·min<sup>-1</sup>). After reduction under the above condition for 120 min, the specimen was cooled to 50 °C and subjected to  $H_2$ -saturation for 30 min in the same atmosphere as above. Then, the atmosphere was switched to the flowing  $N_2$  (30 ml·min<sup>-1</sup>), and the specimen was heated till 500 °C at a rate of 10 °C·min<sup>-1</sup> to desorb the adsorbed  $H_2$ , during which the profile for the change in the signal of  $H_2$  was recorded. In the  $O_2$ -TPO experiment, the specimen was first pre-reduced under the same condition as above in the  $H_2$ -TPD experiment and then cooled to 50 °C. After that, the specimen was purged by  $N_2$

and heated to 500 °C in a flow of 10 % O<sub>2</sub>/Ar (30 ml·min<sup>-1</sup>) for re-oxidization. The change in the signal of O<sub>2</sub> recorded as a function of temperature was thus recorded.

X-ray diffraction (XRD) spectroscopy was measured by a Bruker D8-Advance X-Ray diffraction equipment, under the following conditions: Cu target K $\alpha$  ray ( $\lambda$  = 1.54187 Å); scanning voltage 40 kV, scanning current 40 mA; scanning speed 0.5 s, scanning step 0.02°.

N<sub>2</sub>-physorption experiment was conducted with a Quantachrome Autosorb-1 at liquid-N<sub>2</sub> temperature. Before measurement, the specimen was pretreated at 300 °C for 4 h under vacuum. The BET method was employed to calculate the specific surface area, with the correlation coefficient being above 0.9999. Total pore volume was taken at  $P/P_o = 0.99$ . The “t-plot” method was used to estimate the micropore area, micropore volume and external surface area. The external surface area was evaluated as the sum of mesopore, macropore and crystal external surface areas<sup>43</sup>. Mesoporous pore size was calculated by the model of Barrett-Joyner-Halenda (BJH).

Field emission scanning electron microscopy (FE-SEM) was performed by a JSM 6700F scanning electron microscope. Before measurement, the specimen was ground and ultrasonically dispersed in methanol, and then, loaded on a silicon chip.

X-ray photoelectron spectroscopy (XPS) was performed by a PHI Quantum 2000 XPS system with a monochromatic Al K $\alpha$  source and a charge neutralizer. The binding energy (B.E.) was referenced to the C 1s peak at 284.8 eV of the surface adventitious carbon.

$^{27}\text{Al}$  magic-angle spinning (MAS) NMR spectroscopy was performed by a Bruker DRX-400 spectrometer at room temperature, using a 4 mm MAS broadband probe. Before measurement, the specimen was kept for 12 h in a desiccator containing aqueous sodium chloride solution (1 M, ~ 96 % relative humidity), considering that this hydration protocol could sharpen  $^{27}\text{Al}$  NMR lines by weakening quadrupole interactions<sup>44</sup>. The spectrum obtained was referenced to the octahedral  $\text{Al}^{3+}$  cation in a 1 M aluminum nitrate solution.

Atomic absorption spectroscopy (AAS) was performed by a Varian AA240 apparatus. The specimen was dissolved in aqueous hydrofluoric acid solution using Teflon beaker. Before measurement, the solution was pretreated at 80 °C for 12 h to evaporate the unreacted hydrofluoric acid.

### **3. Results and discussion**

#### **3.1 Characterizations of catalysts**

Fig. 1 shows the changes in the actual Ni loading ( $Ni_A$ ) and yield of Ni loading ( $Y_{Ni}$ ) over Ni/HZSM-5(X) catalysts prepared at various D-P time. One can see that, with increasing the D-P time, the  $Ni_A$  and  $Y_{Ni}$  values first increase steeply, attaining 19.96 wt. % and 99.8 % for a 4 h D-P time, respectively, and then remain these high values for prolonging the D-P time till 24 h. It indicates that after 4 h of D-P, almost all the Ni species in solution have been deposited on the HZSM-5 zeolite, and beyond that D-P time, no more Ni species are available for deposition. The D-P time of 4 h appears to be a watershed, dividing the D-P process into two stages: the first stage (D-P time < 4 h) for the deposition of Ni species and the second stage (D-P time  $\geq$  4 h) probably for the aging of Ni species.

Figure 1

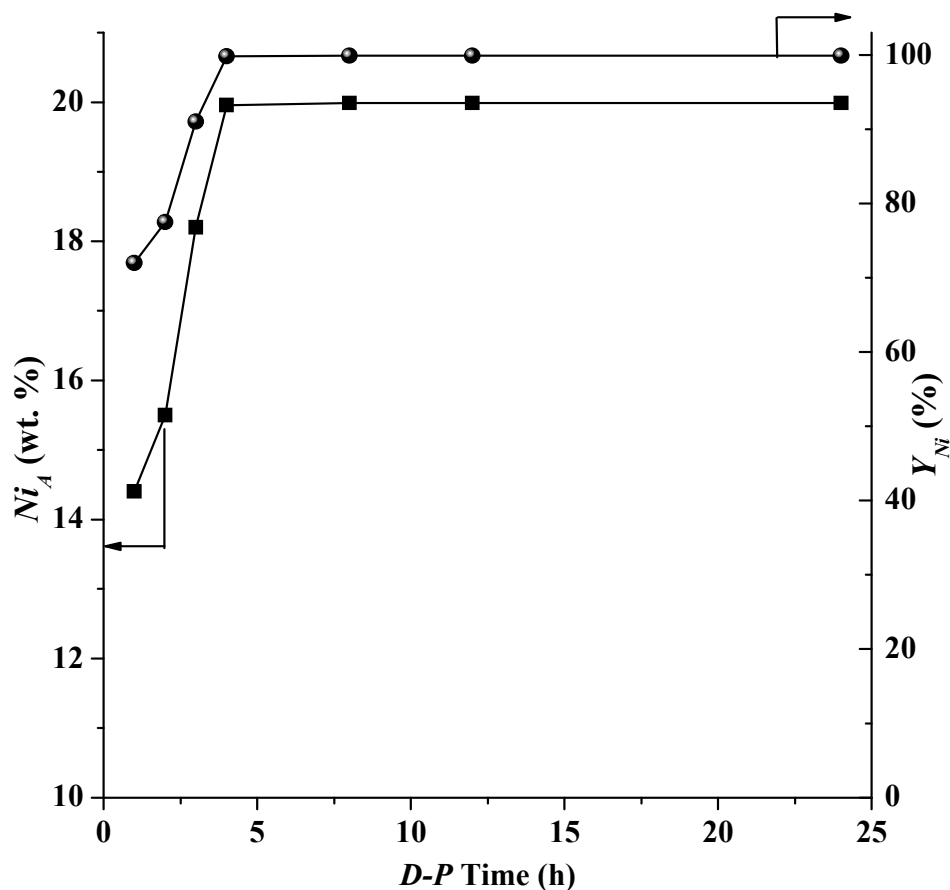


Fig. 1 Actual Ni loading ( $Ni_A$ ) and yield of Ni loading ( $Y_{Ni}$ ) over Ni/HZSM-5(X) catalysts prepared at various D-P time.

Fig. 2 shows the conventional FT-IR spectra for the skeletal vibrations of pure HZSM-5 zeolite and uncalcined Ni/HZSM-5(X) ( $X = 1 \sim 24$ ). All the spectra display the characteristic bands of HZSM-5 at 457, 553, 801, 1109 and 1226  $\text{cm}^{-1}$ , as well as a band at 624  $\text{cm}^{-1}$  probably assigned to the extra-framework low

symmetry  $\text{SiO}_2$ <sup>45</sup>. Besides, a band at  $947\text{ cm}^{-1}$  is identified over the pure HZSM-5 and the bands at  $1005$ ,  $947$ ,  $897$ ,  $673$  and  $637\text{ cm}^{-1}$  over the other specimens. The band at  $947\text{ cm}^{-1}$  can be attributed to the stretching mode of strained doubly bridged structure that possesses a significant atomic polarization in the Si-O-Si bridges<sup>25</sup>. These strained bridges are generated *via* the dehydration of vicinal silanols<sup>9, 11</sup>. It is known that “hydroxyls nests” are clusters of four silanol groups generated from the missing of T atom<sup>25</sup>, and these silanols are in close proximity to each other, being easily suffered from dehydration to generate the strained Si-O-Si bridges at elevated temperature (the HZSM-5 zeolite was calcined at  $550\text{ }^\circ\text{C}$ ; see section 2.1). One can expect that the strained Si-O-Si bridges can be hydrolyzed into hydroxyls in the presence of water. In fact, the band at  $947\text{ cm}^{-1}$  is very unobvious over the Ni-loaded HZSM-5 with a D-P time of 1 h (Fig. 2 b) and disappears gradually with increasing the D-P time (Fig. 2 c ~ g). In this sense, the strained Si-O-Si bridges can be also regarded as an important characteristic of zeolites with abundant “hydroxyls nests”. The band at  $637\text{ cm}^{-1}$  appears for the D-P time of 1 h (Fig. 2 b); with increasing the D-P time, its intensity increases, attaining a maximum for the D-P time of 4 h (Fig. 2 d), and then decreases (Fig. 2 e ~ g). This band can be attributed to the  $\delta_{OH}$  vibration mode of nickel hydroxide deposited over the zeolite surface<sup>31</sup>. The band at  $897\text{ cm}^{-1}$  appears for D-P time of above 2 h (Fig. 2 c ~ g) and those at  $673$  and  $1005\text{ cm}^{-1}$  for D-P time of above 4 h

(Curve 2 d ~ g). All these three bands increase substantially in intensity with increasing the D-P time. As reported in the literature <sup>31, 33</sup>, these three bands are associated with 1:1 nickel phyllosilicate ( $\text{Si}_2\text{Ni}_3\text{O}_5(\text{OH})_4$ , also called nepouite or Ni-lizardite). The bands at 673 and 1005  $\text{cm}^{-1}$  are ascribed to the tetrahedral Si-O mode and Si-O stretching, respectively, in the framework of crystalline 1:1 nickel phyllosilicate <sup>32</sup>, and the band at 897  $\text{cm}^{-1}$ , being a characteristic of ill-crystalline nickel phyllosilicates, is attributed to the Si-O stretching vibration <sup>31</sup>. The above results indicate that, for the uncalcined Ni/HZSM-5(X), during the D-P process, the nickel hydroxide as primary Ni (II) species is first deposited on the zeolite; however, when more nickel hydroxides are deposited, they are gradually transformed into the ill-crystalline nickel phyllosilicates and finally 1:1 nickel phyllosilicates, due to the interaction between the nickel hydroxide and zeolite framework. It supports well the conclusion derived from Fig. 1 that the D-P process consists of two stages, and furthermore, the two stages can be embodied as that, in the first stage (D-P time < 4 h), *i.e.*, deposition of Ni species, the nickel hydroxide is deposited over the zeolite and transformed into the ill-crystalline nickel phyllosilicate, and in the second stage ( $\geq 4$  h), *i.e.*, aging of Ni species, the 1:1 nickel phyllosilicate is generated from the ill-crystalline nickel phyllosilicate.

Figure 2

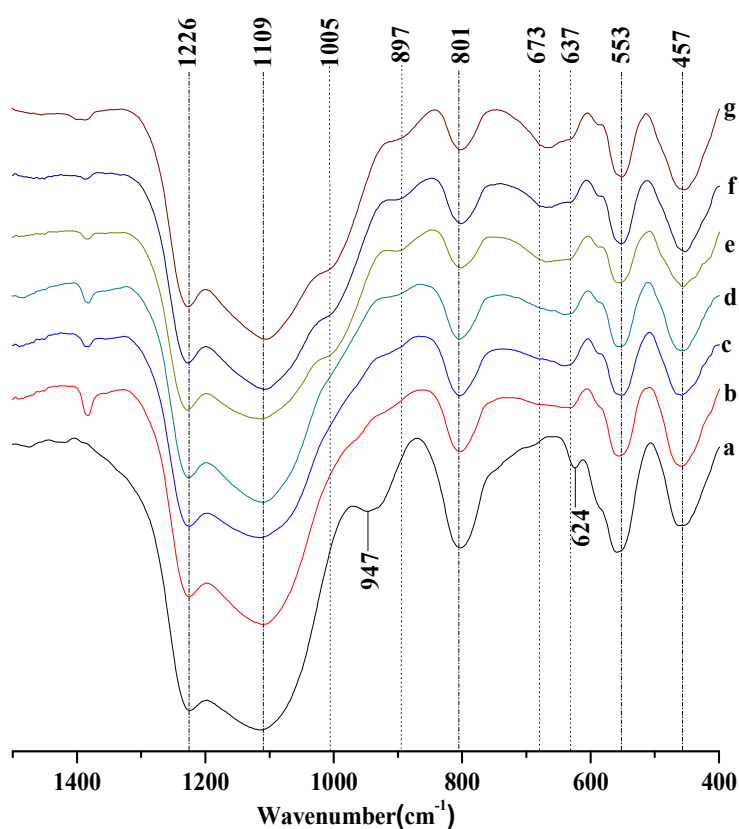


Fig. 2 Conventional FT-IR spectra of HZSM-5 and uncalcined Ni/HZSM-5(X) prepared at various D-P time: (a) HZSM-5; (b) ~ (g), Ni/HZSM-5(X) with D-P time X= 1, 2, 4, 8, 12 and 24 h, respectively.

Fig. 3 shows the FT-IR spectra for the skeletal vibrations of pure HZSM-5 zeolite and calcined Ni/HZSM-5(X) (X = 1 ~ 24 h). One can see that, compared to the uncalcined Ni/HZSM-5(X) (Fig. 2), the band at  $637\text{ cm}^{-1}$  (nickel hydroxide), as well as those at  $673$ ,  $897$  and  $1005\text{ cm}^{-1}$  (1:1 nickel phyllosilicate) disappear, and a

band at  $686\text{ cm}^{-1}$  over all the calcined Ni/HZSM-5(X) (Fig 3 b ~ g) and a band at  $1021\text{ cm}^{-1}$  over the Ni/HZSM-5(X) with  $X > 4$  appear (Fig. 3 e ~ g). With increasing the D-P time, the intensities of both the bands at  $686$  and  $1021\text{ cm}^{-1}$  increase. The band at  $1021\text{ cm}^{-1}$  can be ascribed to the SiO stretching mode for 2:1 nickel phyllosilicate ( $\text{Si}_4\text{Ni}_3\text{O}_{10}(\text{OH})_2$ , also called Ni-talc, kerolite, or willemseite)<sup>31,46</sup>. It was reported that<sup>33</sup>, the 2:1 nickel phyllosilicate exhibited a doublet at  $670$  and  $710\text{ cm}^{-1}$ , which was assigned respectively to the tetrahedral SiO mode ( $670\text{ cm}^{-1}$ ) and  $\delta_{\text{OH}}$  vibration of isolated OH surrounded by three Ni atoms ( $710\text{ cm}^{-1}$ ), while the 1:1 nickel phyllosilicate exhibited an adsorption at  $670\text{ cm}^{-1}$ . Therefore, the band at  $686\text{ cm}^{-1}$  might be caused by a mixture of 1:1 nickel phyllosilicate and 2:1 nickel phyllosilicate. In considering that almost no adsorption at  $1021\text{ cm}^{-1}$  is observed for the D-P time  $\leq 4$  and the intensity of the band at  $686\text{ cm}^{-1}$  is obviously larger for the D-P time  $> 4$  h than for the D-P time  $\leq 4$  h, it is reasonable to deduce that the Ni/HZSM-5(X) with  $X \leq 4$  contain mainly the 1:1 nickel phyllosilicate and the Ni/HZSM-5(X) with  $X > 4$  contain predominantly the 2:1 nickel phyllosilicate. From Fig. 3, one can also see that, the band at  $947\text{ cm}^{-1}$  is observed for the shorter D-P time and decreases in intensity till disappearance with increasing the D-P time. As has been pointed out in the discussion of Fig. 2, the  $947\text{ cm}^{-1}$  is related to the stretching mode of strained doubly bridged structure generated *via* the dehydration of vicinal silanols. Therefore, it appears that the vicinal silanols have taken part in

the generation of nickel phyllosilicates over the HZSM-5 zeolite. For the shorter D-P time, the nickel species have not been completely deposit-precipitated over the HZSM-5, leaving a proportion of vicinal silanols to be intact. With increasing the D-P time, vicinal silanols are consumed in the generation of nickel phyllosilicates. Comparing Fig. 2 and 3, one can conclude that, after calcination, the nickel hydroxide generated at shorter D-P time and 1:1 nickel phyllosilicate formed at longer D-P time may be transformed respectively to the 1:1 nickel phyllosilicate and 2:1 nickel phyllosilicate. It should be mentioned that a proportion of nickel hydroxide may be also possible to be decomposed into nickel oxide, since its decomposition temperature ( $\sim 250$  °C) is lower than the temperature for catalyst calcination (450 °C). However, the adsorption for nickel oxide is very close to that for ZSM-5, being very hard to discriminate from each other.

Figure 3

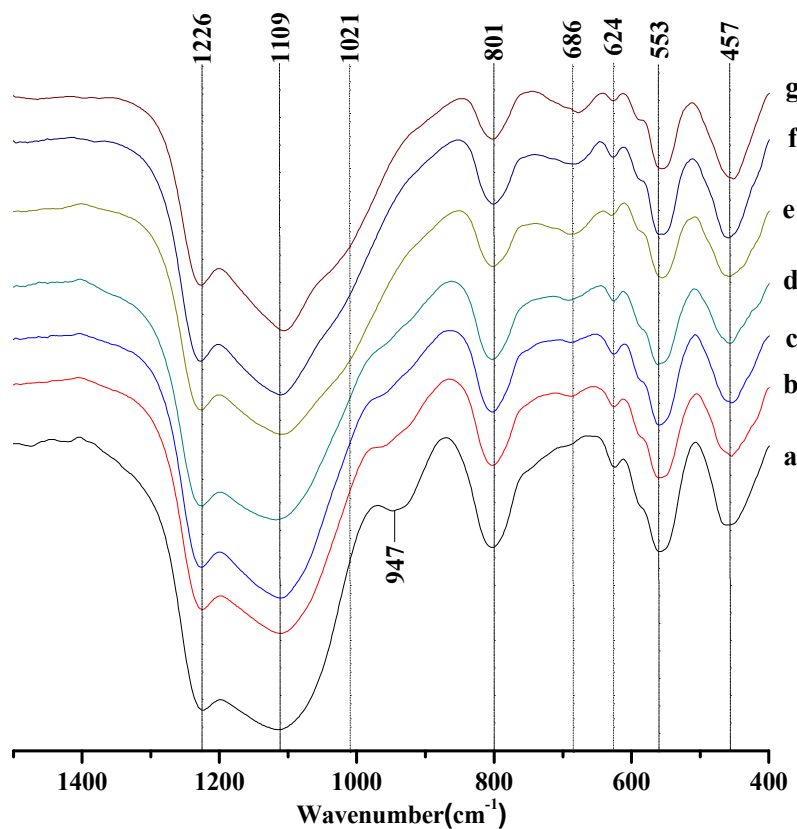


Fig. 3 Conventional FT-IR spectra of HZSM-5 and calcined Ni/HZSM-5(X) prepared at various D-P time: (a) HZSM-5; (b) ~ (g), Ni/HZSM-5(X) with D-P time X= 1, 2, 4, 8, 12 and 24 h, respectively.

Fig. 4 shows the DRS UV-Vis absorbance spectra of pure HZSM-5 as well as the uncalcined and calcined Ni-HZSM-5(X) specimens. It is known that, the Ni(II) ion ( $d^8$  ion) in octahedral crystal field usually exhibits four characteristic electronic

transitions, including three spin-allowed transitions  ${}^3A_{2g}({}^3F) \rightarrow {}^3T_{1g}({}^3P)$ ,  ${}^3A_{2g}({}^3F) \rightarrow {}^3T_{1g}({}^3F)$  and  ${}^3A_{2g}({}^3F) \rightarrow {}^3T_{2g}({}^3F)$  and one spin-forbidden transition  ${}^3A_{2g}({}^3F) \rightarrow {}^1E_g({}^1D)$  <sup>46</sup>. The former three transitions are designed as v1, v2 and v3 bands, respectively, and the last one appears as the shoulder of the v2 band. Over the nickel oxide, additional three spin-forbidden transitions  ${}^3A_{2g}({}^3F) \rightarrow {}^1T_{2g}$ ,  ${}^3A_{2g}({}^3F) \rightarrow {}^1A_{1g}(D)$  and  ${}^3A_{2g}({}^3F) \rightarrow {}^1T_{1g}(D)$ , besides  ${}^3A_{2g}({}^3F) \rightarrow {}^1E_g({}^1D)$ , are also present, due to the specific spin-orbit couplings and antiferromagnetic interactions occurring between Ni(II) ions <sup>47</sup>. Table 1 summarized the electronic transitions, reported in the literature, over various Ni-bearing silicates as well as Ni(OH)<sub>2</sub> and NiO. From Fig. 4, one can see that only one band centered at 233 nm is present over the pure HZSM-5 (Fig. 4 a), and this band can be ascribed to the surface defects <sup>48, 49</sup>. Over the uncalcined Ni/HZSM-5(X), four bands centered at 243, 389, 665 and 750 nm, respectively, are present (Fig. 4 b ~ e). The band at 243 nm can be ascribed to the charge-transfer transitions (C-T band) from oxygen to Ni(II) ion <sup>50, 51</sup>, and the other three bands respectively to the d-d electronic transitions  ${}^3A_{2g}({}^3F) \rightarrow {}^3T_{1g}({}^3P)$ ,  ${}^3A_{2g}({}^3F) \rightarrow {}^3T_{1g}({}^3F)$ , and  ${}^3A_{2g}({}^3F) \rightarrow {}^1E_g({}^1D)$  of Ni(II) in either Ni(OH) or 1:1 nickel phyllosilicate <sup>46, 51-55</sup>. Over the calcined Ni/HZSM-5(X), four bands centered at 276, 457, 660 and 730 nm, respectively, are present for D-P time  $\leq 4$  h (Fig. 4 f ~ g). The band at 276 nm can be assigned to the charge-transfer transitions from oxygen

to Ni(II) and the band at 457 nm to the spin-forbidden transitions  ${}^3A_{2g}({}^3F) \rightarrow {}^1T_{2g}$  of Ni(II) in NiO<sup>53, 56</sup>, while the bands at 660 and 730 nm are ascribed to the d-d electronic transitions  ${}^3A_{2g}({}^3F) \rightarrow {}^3T_{1g}(F)$  and  ${}^3A_{2g}({}^3F) \rightarrow {}^1E_g({}^1D)$  of Ni(II), respectively, in 2:1 nickel phyllosilicate<sup>46</sup>. With increasing the D-P time beyond 4 h (Fig. 4 h ~ i), the bands at 276 and 457 nm shift respectively to 243 and 411 nm, while both the bands at 660 and 730 nm increase in intensity. The bands at 243 and 411 nm can be assigned to the charge-transfer transitions from oxygen to Ni(II) and d-d electronic transitions  ${}^3A_{2g}({}^3F) \rightarrow {}^3T_{1g}(P)$  of Ni(II), respectively, in 2:1 nickel phyllosilicate<sup>46</sup>. The same adsorption wavelength for charge-transfer transitions from oxygen to Ni(II) in the 2:1 nickel phyllosilicate (Fig. 4 f ~ i) as that in the 1:1 nickel phyllosilicate (Fig. 4 b ~ e) is probably due to the fact that both the two nickel phyllosilicates have a lamellar structure. The above phenomena indicate that, (1) the D-P process consists of two stages; (2) the deposit-precipitated nickel hydroxide is transformed into nickel phyllosilicate with increasing the D-P time; (3) the deposit-precipitated nickel hydroxide and 1:1 nickel phyllosilicate are transformed into nickel oxide and 2:1 nickel phyllosilicate, respectively, after calcination. It confirms further the conclusions drawn from Fig. 1 ~ 3.

Figure 4

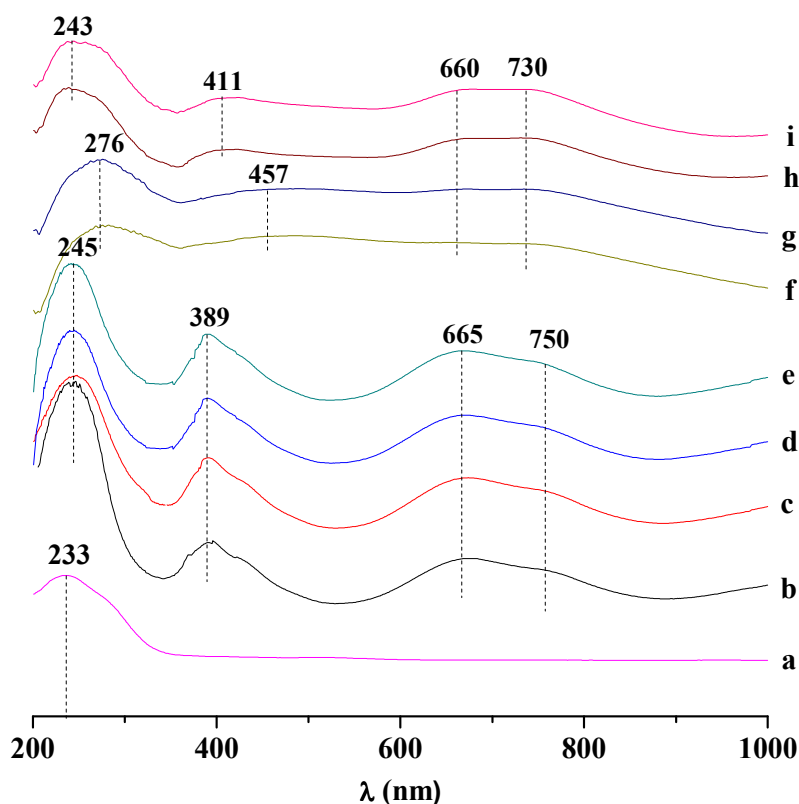


Fig. 4 (i) UV-Vis spectra of HZSM-5; uncalcined 20Ni-HZSM-5(X), X = (b) 2, (c) 4, (d) 12 and (e) 24, respectively; and calcined 20Ni-HZSM-5(X), X = (f) 2, (g) 4, (h) 12, (i) 24, respectively.

Fig. 5 shows the  $H_2$ -TPR profiles of calcined Ni/HZSM-5(X) (X = 1 ~ 24 h). For the D-P time of 1 h (Fig. 5 a), a sharp peak centered at 373 °C and a small peak at 488 °C as the shoulder of the former can be identified. The low-temperature peak is ascribed to the nickel oxide clusters or particle agglomerates, which are

generated from the decomposition of nickel hydroxides, being dispersed highly over the surface of zeolite and thus reducible at relatively low temperature<sup>57, 58</sup>. The high-temperature peak can be assigned to the 2:1 nickel phyllosilicate<sup>31</sup>. For a longer D-P time, the above two peaks merge into one peak, of which both the area and desorption temperature increase with increasing the D-P time (Fig. 5 b ~ d). It occurs probably due to the fact that, with increasing the D-P time, more nickel species deposited over the zeolite are available for the generation of 2:1 nickel phyllosilicate, and therefore, both the concentration and crystallinity (or dimension) of 2:1 nickel phyllosilicate increase<sup>29, 31</sup>. This result is well consistent with that derived from Fig. 3. The 2:1 nickel phyllosilicate with a larger crystallinity (or dimension) requires a higher reduction temperature than those with a smaller crystallinity (or dimension), most probably due to the higher crystal stabilization energy for the former relative to the latter.

Figure 5

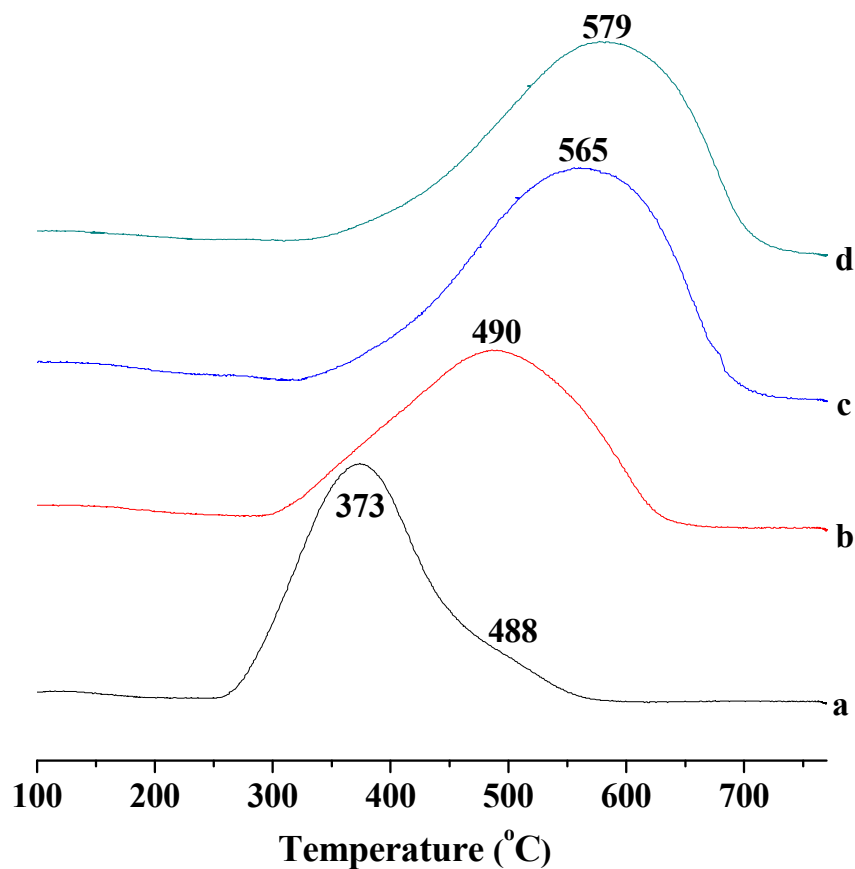


Fig. 5 H<sub>2</sub>-TPR profiles of Ni/HZSM-5(X) prepared at various D-P time, X = (a) 1 h, (b) 4 h, (c) 12 h, and (d) 24 h.

Fig. 6 shows the XRD patterns of HZSM-5 zeolite and calcined Ni/HZSM-5(X) (X = 1 ~ 12 h). All the XRD patterns display a set of diffractions at  $2\theta = 7.9^\circ$ ,  $8.8^\circ$ ,  $23.0^\circ$ ,  $23.2^\circ$ ,  $23.6^\circ$ ,  $23.9^\circ$  and  $24.4^\circ$ , being characteristics of ZSM-5 zeolite,

and their intensities change very little with increasing the D-P time. It indicates that all the Ni/HZSM-5(X) catalysts possess the ZSM-5 structure, which has a nearly negligible change during the D-P process. For a D-P time of 1 h (Fig. 6 b), an additional set of diffraction peaks at  $2\theta = 37.1^\circ$ ,  $43.2^\circ$ , and  $62.8^\circ$  are identified, and these diffraction peaks can be assigned to NiO (JCPDS No 65-6920). With increasing the D-P time, the intensity of diffraction peaks for NiO increases, attaining a maximum for the D-P time of 4 h (Fig. 6 d), and then decreases obviously till near disappearance. This occurs due to the fact that, as has been obtained from Fig. 1 ~ 4, in the first stage of D-P process, nickel hydroxides are deposited over the zeolite and then decomposed into NiO by calcination, and with prolonging the D-P time, more nickel hydroxides and thus more NiO are generated. In the second stage, no more nickel hydroxides are deposited, and meanwhile, nickel hydroxides are transformed into nickel phyllosilicates *via* their interactions with the framework of zeolite. However, one may have observed that no detectable diffractions relating to nickel phyllosilicates are present in the XRD patterns of Ni/HZSM-5(X). It implies that the nickel phyllosilicates may most probably have a high dispersion in the catalysts.

Figure 6

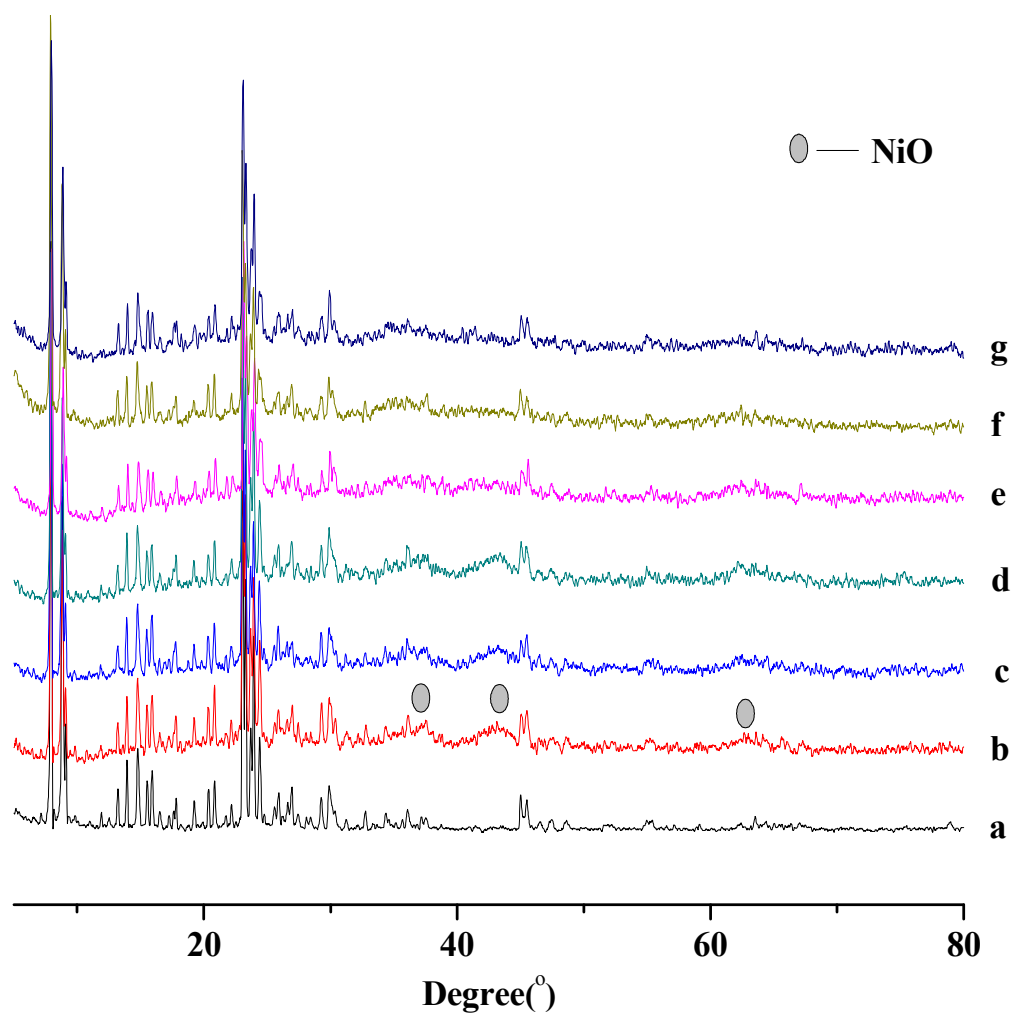


Fig. 6 XRD patterns of HZSM-5 and Ni/HZSM-5(X) prepared at various D-P time: (a) HZSM-5; (b) ~ (g), Ni/HZSM-5(X) with D-P time X = 1, 2, 4, 8, 12 and 24 h, respectively.

Fig. 7 shows the change in the dispersion of metal nickel in calcined Ni/HZSM-5(X) (X = 1 ~ 24 h) as a function of D-P time. The dispersion of metallic nickel has been estimated as follows <sup>59</sup>:

$$D_{actual} (\%) = \frac{\text{No. of Ni}^0 \text{ atoms on surface}}{(\text{Total No. of Ni atoms})(\text{Fraction reduced})} \times 100\% \quad (\text{Eq. 1})$$

where the *No. of Ni<sup>0</sup> atoms on surface* is provided by the surface metal Ni density ( $10^{20}$  atoms/g catalyst) obtained from H<sub>2</sub>-TPD basing on a H/Ni = 1 stoichiometric atomic ratio <sup>60</sup>, the *fraction reduced* is provided by the reduction degree of Ni obtained from O<sub>2</sub>-TPO, and the *Total No. of Ni atoms* is provided by the actual Ni loading ( $Ni_A$ ) from Fig. 1. The related surface metallic nickel density and reduction degree of nickel for the Ni/HZSM-5(X) are listed in Table 2. One can see that, with increasing the D-P time, the reduction degree decreases, while the surface metallic nickel density decreases first, attending its minimum for D-P time of 4 h, and then increases. The above result occurs due to the fact that, for the D-P time < 4 h, nickel hydroxides are gradually deposited and then decomposed into NiO upon calcination; meanwhile, small amount of nickel phyllosilicates can be also generated *via* the interaction of nickel hydroxides with ZSM-5 framework. Since the NiO formed by the decomposition of nickel hydroxides have larger reduction susceptibility than the nickel phyllosilicates (see Fig. 5), it can be more easily reduced. This leads to the decrease in both the reduction degree of nickel species

and surface metallic Ni density, with increasing the D-P time. For the D-P time  $\geq 4$  h, the Ni loading approaches its theoretical largest value, and thus, no more Ni species are available for deposition. In this case, more nickel phyllosilicates with higher crystallinity (or dimension) are generated from the Ni species already deposited over the zeolite, with increasing the D-P time. This decreases the reduction degree of nickel species but increases the surface metallic Ni density due to the separation of metallic Ni by the nickel phyllosilicates. The above variations in both the reduction degree of nickel species and surface metallic Ni density decide that the dispersion of metallic nickel, calculated according to Eq. 1, increases with increasing the D-P time. This is of considerably large importance for the application of Ni/HZSM-5 as hydrogenation catalyst, since a high dispersion of metallic Ni as active site is more favorable to the activations of hydrogen and hydrocarbons, compared to a low dispersion of metallic Ni.

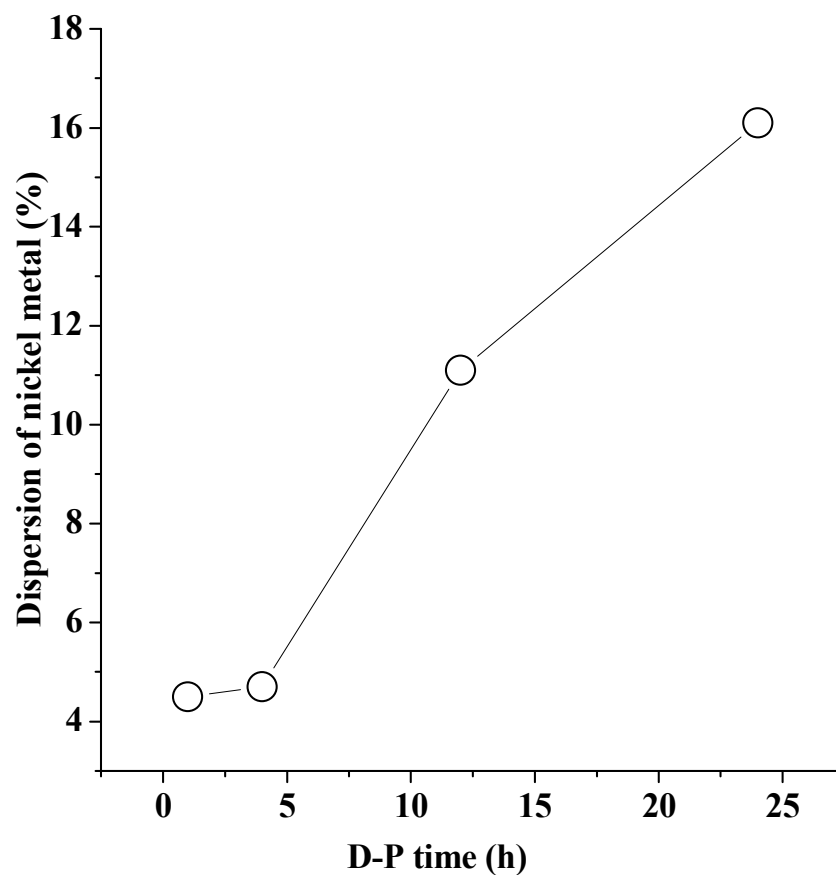
**Figure 7**

Fig. 7 Change in the dispersion of nickel as a function of D-P time (h).

Fig. 8 shows the  $N_2$  adsorption/desorption isotherms of HZSM-5 and Ni/HZSM-5(X) (X = 1 ~ 24 h). One can see that all the isotherms rise steeply at the very low  $P/P_0$ , being an indication of the presence of micropores in these catalysts. In addition, an obvious hysteresis loop at the  $P/P_0 > 0.4$  is present for all

the Ni/HZSM-5(X) catalysts (Fig. 8 b ~ g), but almost absent for the pure HZSM-5 zeolite (Fig. 8 a), indicating that mesopores are introduced in the Ni/HZSM-5(X) catalysts during the D-P process<sup>61</sup>. All the hysteresis loops belong to the type H3 in the IUPAC classification, suggesting that the mesopores in the Ni/HZSM-5(X) catalysts have the complex and irregular shapes, *e.g.*, long and narrow slit-pores<sup>62</sup>, similar as those in the solids consisting of aggregates or agglomerates of plates or edged particles<sup>63, 64</sup>. The hysteresis loops for the Ni/HZSM-5(X) catalysts with a longer D-P time ( $X \geq 4$ ) are found to be larger than those with a relative short D-P time ( $X < 4$ ). It indicates that the prolonging of D-P time increases the mesoporosity in the Ni/HZSM-5(X) catalysts.

Figure 8

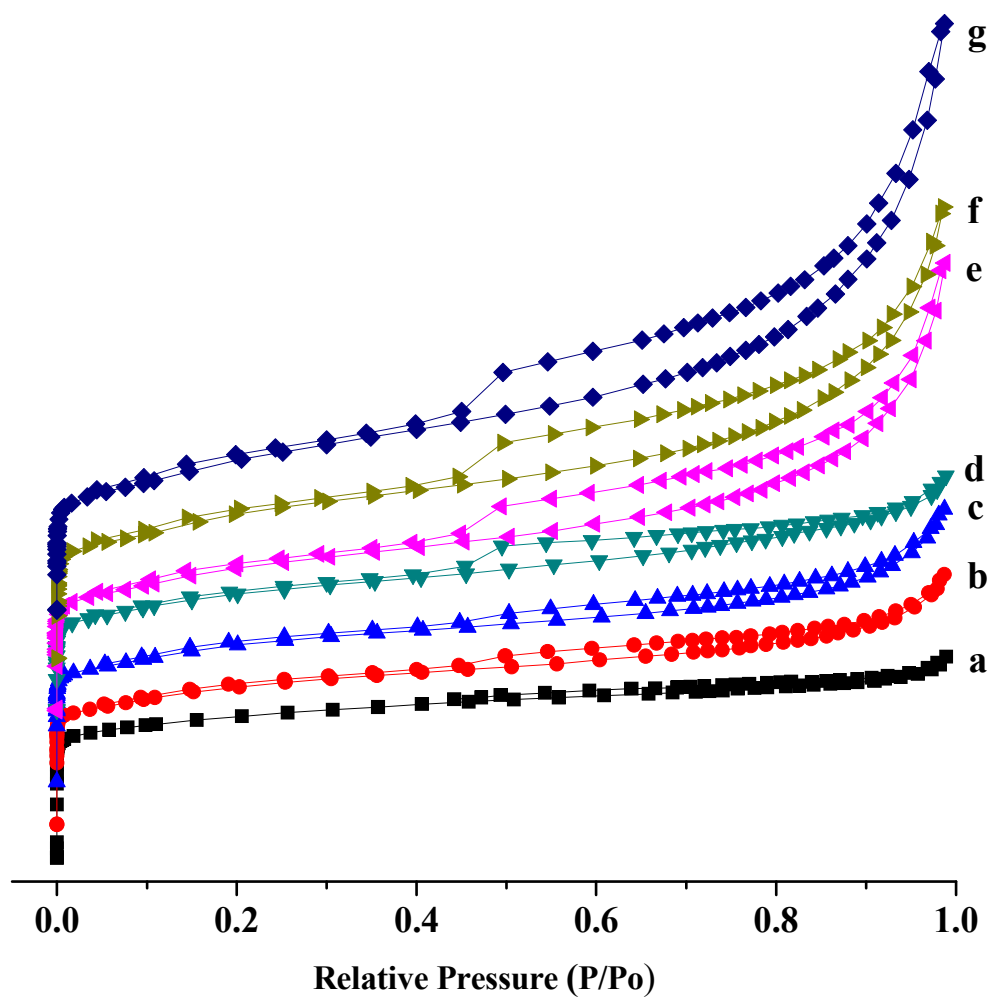


Fig. 8  $N_2$  adsorption/desorption isotherms of HZSM-5 and Ni/HZSM-5(X) prepared at various D-P time: (a) HZSM-5; (b) ~ (g), Ni/HZSM-5(X) with D-P time  $X = 1, 2, 4, 8, 12$  and  $24$  h, respectively.

The main textural properties of both the HZSM-5 and Ni/HZSM-5(X) catalysts prepared at various D-P time are listed in Table 3. One can see that, the average pore size of mesopores in the Ni/HZSM-5(X) catalysts increases in the range of 16.7 ~ 19.5 Å, with increasing the D-P time. Compared to the pure HZSM-5, the Ni/HZSM-5(1) possesses a larger mesopore volume ( $V_{pore,mes}$ ), total pore volume ( $V_{pore,t}$ ), external surface area ( $S_{ext}$ ) and average mesopore size ( $D_{pore,ave}$ ), but a smaller micropore volume ( $V_{pore,mic}$ ), micropore surface ( $S_{mic}$ ) and specific surface area ( $S_{BET}$ ). With increasing the D-P time, the  $V_{pore,mes}$ ,  $S_{ext}$  and  $D_{pore,mes}$  increase slightly and the  $V_{pore,mic}$  and  $S_{mic}$  decrease largely for the D-P time  $\leq 4$  h; however, when the D-P time  $> 4$ h, the increases in the  $V_{pore,mes}$ ,  $S_{ext}$  and  $D_{pore,mes}$  become large and the decreases in the  $V_{pore,mic}$  and  $S_{mic}$  turn to be small. As the results of the above variations in the mesoporosity and microporosity, the  $S_{BET}$  decreases first, attending its minimum at the D-P of 4 h, and then increases, while the  $V_{pore,t}$  remains unchanged for the D-P time  $\leq 4$  h and increases obviously with the D-P time increasing beyond 4 h. The above variation in the microporosity occurs most probably due to the fact that, during the D-P process, the deposited Ni species block partially the micropores of HZSM-5 zeolite, and the circumstance becomes serious with increasing the D-P time within 4 h, as more nickel species being deposited on the HZSM-5 zeolite; however, for the D-P time longer than 4 h, the nickel species have been completely deposited on the HZSM-5 zeolite and the

nickel phyllosilicates are generated *via* the interaction between the nickel species and silicon species dissolved from the zeolite<sup>29</sup>. It is reasonable that a small proportion of dissolved silicon species are deposited on the micropores of HZSM-5 zeolite, while the most proportion of dissolved silicon species are reacted with nickel species to form the nickel phyllosilicates. Therefore, although no more nickel species are deposited on the HZSM-5 zeolite for the D-P time longer than 4 h, the microporosity of HZSM-5 decreases. With increasing the D-P time, more dissolved silicon species are deposited in the microporous; it leads to a remarkable decrease in the microporosity. The generation of mesopores in the Ni/HZSM-5 catalyst and variation in the mesoporosity with the D-P time are most probably due to the formation of nickel phyllosilicates in the catalysts. As pointed above, the formation of nickel phyllosilicates involves the dissolution of silicon from the framework of HZSM-5 zeolite, leaving defects in the zeolite, and the interaction between the dissolved silicon species and nickel species. Therefore, several of the above defects may move, aggregate and merge into a large one, leading to the formation of mesopores in the zeolite. During the D-P process, nickel species are gradually deposited on the zeolite and interacted with the framework of zeolite, involving the dissolution of silicon as intermediate step, to generate small amounts of nickel phyllosilicates. This leads to the small increase in the mesoporosity in the catalysts for the D-P time within 4 h. For the D-P time longer than 4 h, no more

nickel species are available for deposition, and the main process occurred is the transformation of the deposited nickel species into the nickel phyllosilicates. With increasing the D-P time, more nickel phyllosilicates are generated, requiring more dissolved silicon species, and thus, the mesoporosity increases obviously in the catalysts. It should be mentioned that the generation of nickel phyllosilicates and mesopores have not altered obviously the structure of HZSM-5, as evidenced by the XRD and FT-IT results (see Fig. 2, 3 and 6).

Fig. 9 shows the FE-SEM micrographs of calcined Ni/HZSM-5(X) (X = 1 ~ 24 h). The HZSM-5 zeolite consists of crystal with clean surface (see ESI, Fig. S1). After D-P of nickel species for 1 h (Fig. 9 a) , the surface of zeolite crystal becomes coarse, over which the NiO with morphologies of irregular leafs or agglomeration particles, generated from the decomposition of deposited nickel hydroxides<sup>65, 66</sup>, can be obviously identified. This observation is well consistent with that reported in the literature<sup>65, 66</sup>. With increasing the D-P time (Fig. 9 b ~ d), the amount of the above irregular leafs and agglomeration particles decreases, and the surface of zeolite crystal becomes relative smooth. This occurs most probably due to the fact that the deposited nickel species are transformed into the nickel phyllosilicates and the latter are not only well dispersed on the surface but also located in the pores of zeolite crystals. It is worthy to mention that obvious cracks are present in the zeolite crystal for the Ni/HZSM-5(24), and this can be an

evidence for the generation of mesopores due to the interaction between deposited nickel species and HZSM-5 zeolite, as deduced from the N<sub>2</sub>-physisorption results.

**Figure 9**

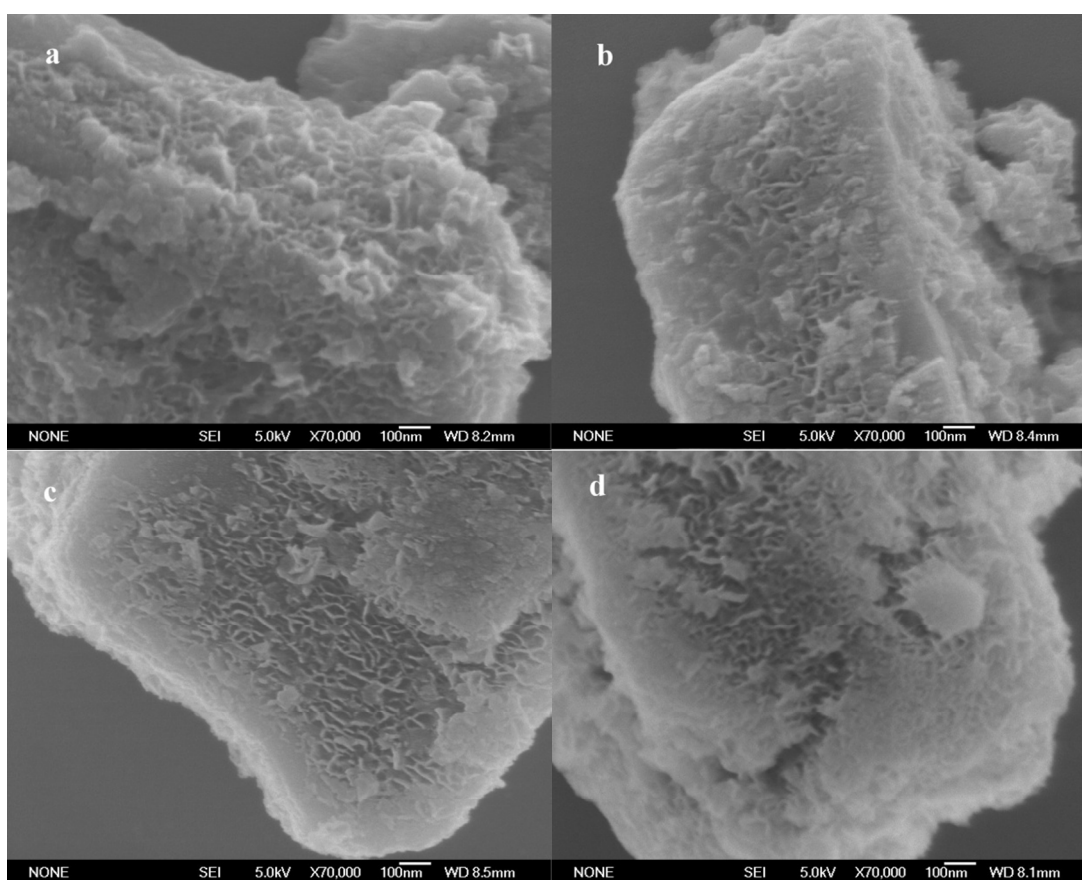


Fig. 9 FE-SEM images of Ni/HZSM-5(X) prepared at various D-P time; D-P time X = (a) 1 h, (b) 4 h, (c) 12 h, and (d) 24 h.

Fig. 10 shows the O 1s and Ni 2p<sub>3/2</sub> XPS spectra for calcined Ni/HZSM-5(X) (X = 1 ~ 24 h). For the Ni/HZSM-5(2), the deconvolution and peak fitting show that the O 1s peak ranging from 528 ~ 535 eV consists of two component peaks with B. E. at *ca.* 529.6 and 531.9 eV, being ascribed to the oxygen ions in the NiO and nickel phyllosilicates, respectively<sup>67-69</sup>, while the Ni 2p<sub>3/2</sub> peak in the range of 850 to 858 eV comprises two component peaks with B. E. at *ca.* 854.4 and 856.3 eV, being assigned respectively to the nickel ions in the NiO and nickel phyllosilicates<sup>67</sup>. With increasing the D-P time, the peaks for NiO decrease and those for nickel phyllosilicates increase. Particularly, for the Ni/HZSM-5(X) prepared at the D-P time larger than 4 h, the peaks related to the NiO are almost absent. It indicates that both the NiO and nickel phyllosilicates are present over the surface of Ni/HZSM-5(X) prepared at the D-P time  $\leq 4$  h; however, mainly the nickel phyllosilicates are present over the surface of Ni/HZSM-5(X) prepared at the D-P time  $> 4$  h.

Figure 10

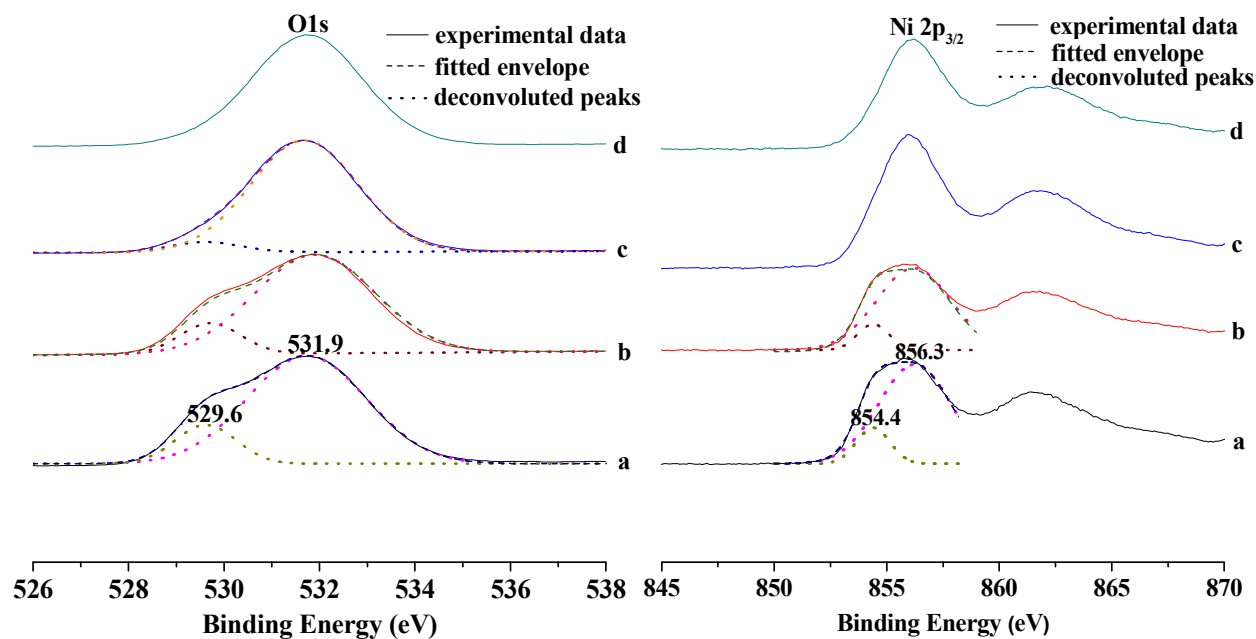


Fig. 10 O1s and Ni2p XPS spectra for Ni/HZSM-5(X) prepared at various D-P time; D-P time X = (a) 2 h, (b) 4 h, (c) 12 h, and (d) 24 h.

Fig. 11 shows the FT-IR spectra in the hydroxyl stretching region ( $4000 \sim 3000 \text{ cm}^{-1}$ ) over the HZSM-5 zeolite as well as the uncalcined and calcined Ni/HZSM-5(4). The specimens have been vacuumed for 8 h under  $10^{-5}$  Torr at  $200^\circ\text{C}$ , before recording the spectra. It is known that, HZSM-5 zeolites, especially highly siliceous ones, contain a high concentration of internal Si-OH groups on the internal surfaces, besides the terminal Si-OH groups on the external surfaces. The internal Si-OH groups can be generated from the acidification of non-intact Si-O-

Si bonds<sup>24</sup>, being the bridges between the silicon atoms from the first and second coordination shells, the decomposition of TPA cations or exchange of Na<sup>+</sup> cations at the Si-O- defect centers with protons<sup>4,24</sup>, as well as the missing of T atoms<sup>25</sup>. In the latter case, “hydroxyl nest”, as a cluster of four silanol groups ( $\equiv\text{Si-OH}$ ), is formed<sup>25</sup>. The “hydroxyls nests” can group together to form chains with variable length and shape and their aggregation generates internal hydroxylated mesopores or nanocavities, while the combination of mesopores leads to the channels and cracks, which outline the boundaries of fractured crystallite fragments<sup>70</sup>. The IR bands for the terminal Si-OH groups located on the external surfaces appear at 3740 ~ 3800 cm<sup>-1</sup> and those for the internal Si-OH groups have wavenumbers below 3740 till 3300 cm<sup>-1</sup><sup>4, 6, 8, 9, 19, 41, 71, 72</sup>. The mutual interactions of hydrogen bonds between the proximate Si-OH groups lead to the broadening of IR bands and their shifting towards lower wavenumbers<sup>8</sup>. In present work, over the pure HZSM-5, the bands at 3721, 3699, 3666 and 3607 cm<sup>-1</sup> as well as a broad and strong band at 3450 cm<sup>-1</sup> are identified (Fig. 11 a). The band at 3721 are assigned to the isolated Si-OH groups located at internal sites<sup>8, 71, 73</sup> and that at 3699 cm<sup>-1</sup> to the “hydroxyls nests”<sup>6</sup>. Both the bands at 3666 and 3450 cm<sup>-1</sup> are related to the clusters of internal Si-OH groups involved in the delocalized hydrogen-bonded linear and ring chains<sup>6</sup>, with the band at 3666 cm<sup>-1</sup> being ascribed to the clusters of internal Si-OH groups with a smaller dimension and that at 3450 cm<sup>-1</sup> to the larger

one<sup>8</sup>. The high intensity and large width of the 3450 cm<sup>-1</sup> band can be rationalized by the presence of a high concentration of internal hydroxylated cavities with considerably large dimension in the zeolite framework. It is also possible that the 3666 cm<sup>-1</sup> band is associated with the extra-framework Al-OH groups over the surface of small Al<sub>2</sub>O<sub>3</sub> clusters, generated by dehydroxylation<sup>41, 74</sup>. The band at 3607 cm<sup>-1</sup> can be assigned to the bridged (SiOHAl) hydroxyl groups, *i.e.*, the strong Brönsted acidic sites<sup>19</sup>. Compared to the pure HZSM-5, over the uncalcined Ni/HZSM-5(4) (Fig. 11 b), the bands at 3721 and 3699 cm<sup>-1</sup> are still present, with the intensity of the former remaining almost unchanged and that of the latter decreasing largely; however, the bands at 3666, 3607 and 3450 cm<sup>-1</sup> disappear. Meanwhile, a new band at 3640 cm<sup>-1</sup> and two bands at 3500 and 3385 cm<sup>-1</sup> appear. As has been obtained from Fig. 2, both the nickel hydroxides and 1:1 nickel phyllosilicate are present over the uncalcined Ni/HZSM-5(4). The band at 3640 cm<sup>-1</sup> in Fig. 11 b can be ascribed to the  $\nu_{\text{OH}}$  vibration associated to the nickel hydroxide and / or the octahedral-coordinated Ni(II) in the brucite-type sheet of 1:1 nickel phyllosilicate<sup>31, 33</sup>, while the band at 3500 cm<sup>-1</sup> is associated with the hydrogen-bonded hydroxyls groups from the nickel hydroxide<sup>75</sup>. The band at 3385 cm<sup>-1</sup> is probably due to the intercalated physisorbed water molecules in lamellar nickel hydroxides<sup>76</sup>. The above results suggest that there are different levels of interactions between nickel species and hydroxyl groups. The interaction of nickel

species with the internal S-OH groups leads to the formation of 1:1 nickel phyllosilicate, to which the internal Si-OH groups involved in the delocalized hydrogen-bonded linear and ring chains, which locate in the mesopores or nanocavities generated *via* the aggregations of “hydroxyls nests”, contribute predominantly, the single “hydroxyls nests” relatively less, but the isolated internal Si-OH groups very little. It seems that the accessibility of internal Si-OH group, *i.e.*, steric effect, affects significantly the formation of 1:1 nickel phyllosilicates. The interaction between nickel species and the extra-framework Al-OH groups generates the non-stoichiometric or spinel type Al-Ni oxides<sup>22</sup>. The interaction between nickel species and the bridged Si(OH)Al hydroxyl groups is still uncertain, because the above disappearance of the band at 3607 cm<sup>-1</sup> can be also due to its overshadowing by the relatively broad and strong band at 3640 cm<sup>-1</sup>. After the calcination of Ni/HZSM-5(4) (Fig. 11 c), both the bands at 3721 and 3699 cm<sup>-1</sup> remain nearly unchanged in intensity, indicating the isolated internal Si-OH groups and “hydroxyls nests” are intact, and the bands at 3500 and 3385 cm<sup>-1</sup> disappear due to the decomposition of nickel hydroxides and desorption of intercalated physisorbed water molecules in lamellar nickel hydroxides, respectively. Besides, the band at 3640 cm<sup>-1</sup> disappears, but a new band at 3622 cm<sup>-1</sup>, being attributed to 2:1 nickel phyllosilicate<sup>33</sup>, appears. It indicates that the calcination leads to the transformation of the nickel hydroxide and 1:1 nickel phyllosilicate to the 2:1

nickel phyllosilicate. One may note that the band at *ca.*  $3740\text{ cm}^{-1}$ , being characteristic of isolated terminal silanol on the external surface of HZSM-5 zeolite <sup>4, 77</sup>, does not appear over not only the pure HZSM-5 but also Ni/HZSM-5(4). This occurs most probably due to the fact that the  $3700 \sim 3800\text{ cm}^{-1}$  interval covers the adsorptions of few other external Si-OH groups, *e.g.*, germinal silanol <sup>78</sup>, and even silanol groups with physically adsorbed water, besides that for the isolated terminal silanol. Thus, the band at  $3740\text{ cm}^{-1}$  is overshadowed by the complex adsorption in above region <sup>8</sup>.

Figure 11

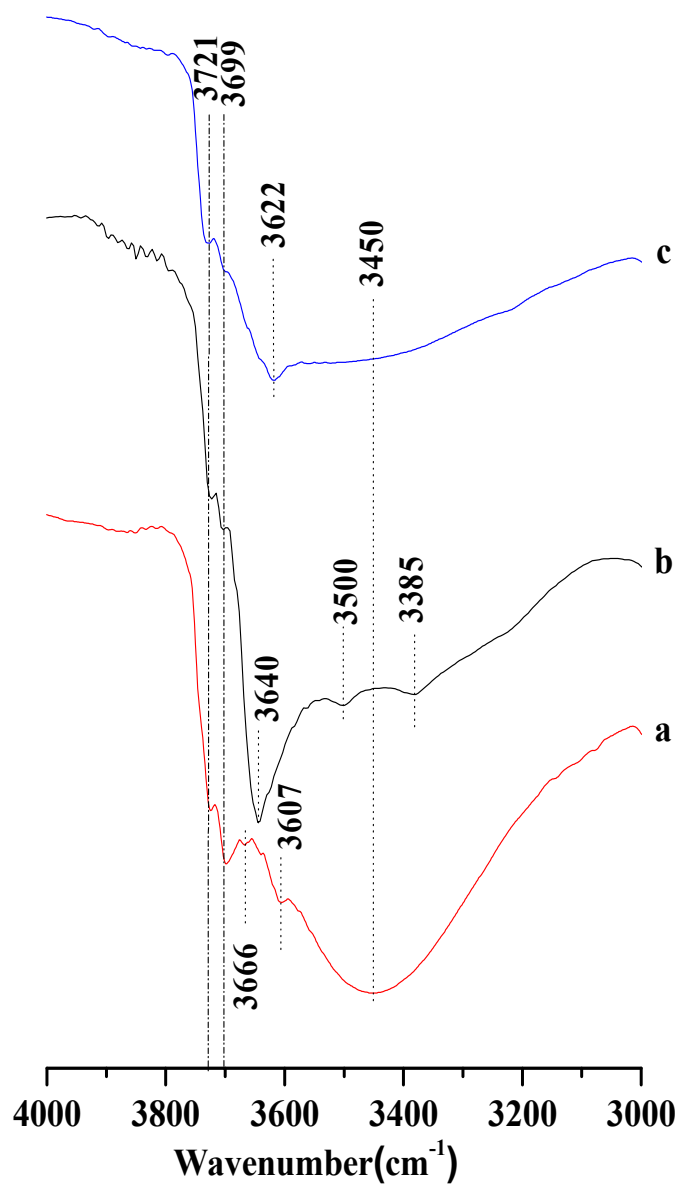


Fig. 11 Vacuum FT-IR spectra over (a) HZSM-5, (b) uncalcined Ni/HZSM-5(4) and (c) Ni/HZSM-5(4) (The specimens are vacuumed for 8 h under  $10^{-5}$  Torr at 200 °C).

Fig. 12 shows the FT-IR spectra in the hydroxyl stretching region ( $4000 \sim 3000 \text{ cm}^{-1}$ ) over the HZSM-5 zeolite and calcined Ni/HZSM-5(X) ( $X = 1 \sim 24 \text{ h}$ ). The specimens have been vacuumed for 8 h under  $10^{-5}$  Torr at  $400 \text{ }^\circ\text{C}$ , before recording the spectra. One can see that, the sharp bands at  $3721$ ,  $3699$ ,  $3666$ ,  $3607 \text{ cm}^{-1}$  and a broad band at  $3450 \text{ cm}^{-1}$  are present over the pure HZSM-5 vacuumed at  $400 \text{ }^\circ\text{C}$  (Fig. 12 a), being same with those over the pure HZSM-5 vacuumed at  $200 \text{ }^\circ\text{C}$  (Fig. 11 a). It indicates that the increase in the temperature for vacuuming treatment does not change the hydroxyl groups over the pure HZSM-5. Compared to the pure HZSM-5 (Fig. 12 a), over the Ni/HZSM-5(1) (Fig. 12 b), the bands at  $3721$  and  $3607 \text{ cm}^{-1}$  remain unchanged and those at  $3699$  and  $3450 \text{ cm}^{-1}$  decrease, particularly for the  $3450 \text{ cm}^{-1}$  band, while the band at  $3640 \text{ cm}^{-1}$  appears and that at  $3666 \text{ cm}^{-1}$  disappears. It indicates that, after a 1 h of D-P, the 1:1 nickel phyllosilicate (the  $3640 \text{ cm}^{-1}$  band) is generated at the expense of mainly the clusters of internal Si-OH groups involved in the delocalized hydrogen-bonded linear and ring chains (the  $3450 \text{ cm}^{-1}$  band), *i.e.*, Si-OH in the internal hydroxylated cavities, and a proportion of “hydroxyls nests” (the  $3699 \text{ cm}^{-1}$  band). Both the isolated Si-OH groups located at internal sites (the  $3721 \text{ cm}^{-1}$  band) and bridged (SiOHA1) hydroxyl groups (the  $3607 \text{ cm}^{-1}$  band) have a very little interaction with nickel species. However, the extra-framework Al-OH groups (the  $3666 \text{ cm}^{-1}$  band) is completely consumed to generate the non-stoichiometric or spinel type Al-Ni

oxides. With increasing the D-P time to 2 h (Ni/HZSM-5(2), Fig. 12 c), the Si-OH groups present over the Ni/HZSM-5(1) remain unchanged, except that the concentration of the internal Si-OH groups in the internal hydroxylated cavities decreases largely, due to their consumptions in the formation of 1:1 nickel phyllosilicate. With increasing further the D-P time to 4 h (Fig. 12 d) and above (Fig. 12 e ~ g), the band at 3699 keeps stable and those at 3721, 3640, 3607 and 3450  $\text{cm}^{-1}$  disappear completely, and meanwhile, the bands at 3622 and 3740  $\text{cm}^{-1}$  appear. This result indicates that, after nickel species have been completely deposited, the increase in the D-P time does not consume more “hydroxyl nests” (the 3699  $\text{cm}^{-1}$  band) but devour totally the internal Si-OH groups in the internal hydroxylated cavities (the 3450  $\text{cm}^{-1}$  band), due to their interaction with the 1:1 nickel phyllosilicate (the 3640  $\text{cm}^{-1}$  band) to generate the 2:1 nickel phyllosilicate (the 3622  $\text{cm}^{-1}$  band). The disappearance of the 3607  $\text{cm}^{-1}$  band at the D-P time > 4 h may be not due to the interaction between bridged (SiOHAl) hydroxyl groups and nickel species, since its intensity does not change with the D-P time for the D-P time < 4 h; instead, it is probably due to the fact that the band at 3607  $\text{cm}^{-1}$  band is overshadowed by the vicinal band at 3622  $\text{cm}^{-1}$ . This result suggests that the interaction between nickel species and bridged (SiOHAl) hydroxyl groups is considerably weak. The disappearance of isolated internal Si-OH groups (the 3721  $\text{cm}^{-1}$  band) over the Ni/HZSM-5(X) ( $X \geq 4$ , Fig. 12 d ~ g) seems to be related to

either prolonging the D-P time or increasing the temperature for vacuum treatment, because this kind of Si-OH groups are obviously present over both the Ni/HZSM-5(X) with a D-P time < 4 h (Fig. 12 b and c) and Ni/HZSM-5(4) vacuumed at a lower temperature (200 °C) (Fig. 11 c). It was reported that the appearance of isolated internal Si-OH groups was always coupled with the presence of Si-O-Na sites in the vicinity, which could be transformed into Si-OH groups *via* ion-exchange<sup>24</sup>. Because of its less accessibility in the internal defects, the Si-O-Na can be only exchanged by NH<sub>4</sub><sup>+</sup> ions, which are generated from the decomposition of urea, for a relatively long D-P time. After calcination, the Si-O-NH<sub>4</sub> sites are first decomposed into the Si-OH groups, and then subjected to the dehydration with the vicinal Si-OH groups to form the intact Si-O-Si bonds. This accounts for the disappearance of 3721 cm<sup>-1</sup> band over the Ni/HZSM-5(X) prepared at longer D-P time (Fig. 12 d ~ g) than over those prepared at shorter D-P time (Fig. 12 b and c). The absence of 3721 cm<sup>-1</sup> band for vacuum treatment at 400 °C but its presence for vacuum treatment at 200 °C over the Ni/HZSM-5(4) is most probably due to the fact that, during the preparation of catalyst, the calcination (450 °C) has not decomposed completely the Si-O-NH<sub>4</sub> sites, and thus, the further vacuum treatment at 400 °C promotes the decomposition of Si-O-NH<sub>4</sub> sites into the Si-OH groups and subsequent dehydration of Si-OH groups to the intact Si-O-Si bonds. As regard to the band at 3740 cm<sup>-1</sup> for the terminal Si-OH groups on the external

surface, its appearance can be a result of not only prolonging the D-P time (Fig. 12 d ~ g *cf.* Fig. 12 b and c) but also increasing the temperature for vacuum treatment (Fig. 12 d *cf.* Fig. 11 c). As has been obtained from Figs. 2 ~ 4 and 9 ~ 12, the prolonging of D-P time leads to the formation of nickel phyllosilicates *via* the interaction between the deposited nickel species and framework of ZSM-5 zeolite, involving the dissolution of silicon atoms as one of intermediate steps, and in turn, the generation of mesopores in the zeolite crystals (see Fig. 8). Meanwhile, some “hydroxyls nests” and the Si-OH in the internal hydroxylated cavities are consumed obviously (Fig. 12 d ~ g). It hints that, during the formation of nickel phyllosilicates, some unreacted internal Si-OH groups become to be the external ones. In addition, as has been known, the band at  $3740\text{ cm}^{-1}$  can be eclipsed by those for other external Si-OH groups, *e.g.*, germinal silanol groups, hydrogen-bonded silanol groups and even silanol groups with physically adsorbed water<sup>78</sup>. Accordingly, the relatively high temperature for vacuum treatment promotes the dehydrations of the above interstitial Si-OH groups, enabling the isolated external Si-OH groups (the  $3740\text{ cm}^{-1}$  band) to be detectable.

Figure 12

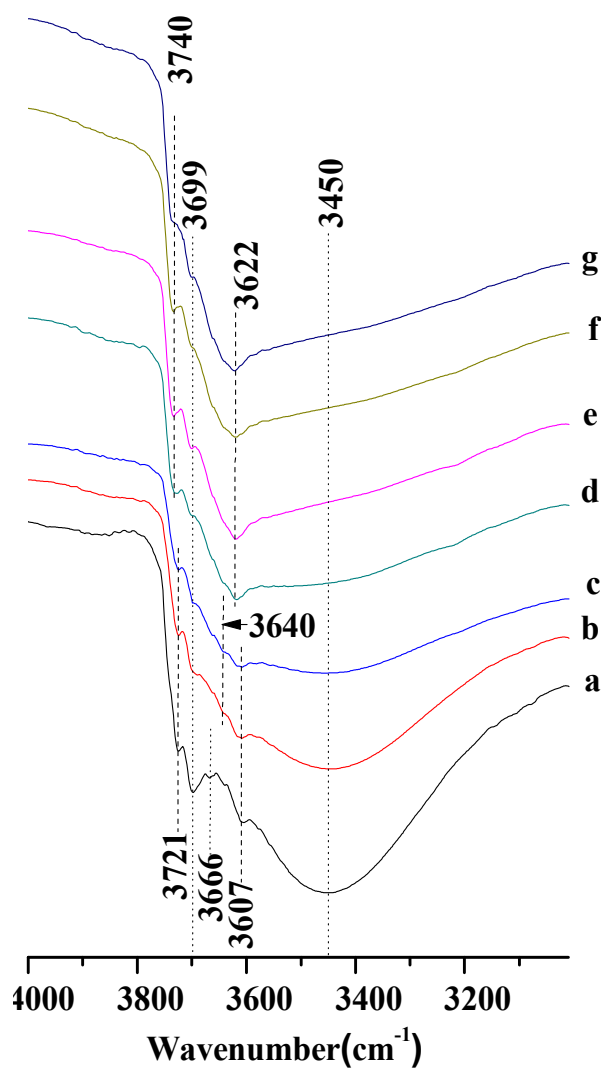


Fig. 12 Vacuum FT-IR spectra of HZSM-5 and Ni/HZSM-5(X) prepared at different D-P time; (a) HZSM-5; (b) ~ (g), D-P time X = 1, 2, 4, 8, 12 and 24 h, respectively (The specimens are vacuumed for 8 h under  $10^{-5}$  Torr at 400 °C).

Fig. 13 shows the pyridine adsorption FT-IR spectra in the 2200 ~ 1200  $\text{cm}^{-1}$  region over HZSM-5, and uncalcined and calcined Ni/HZSM-5(4) catalysts. One can see that two strong peaks of pyridine adsorption located at 1540 and 1450  $\text{cm}^{-1}$ , being respectively ascribed to the Brönsted and Lewis acidic sites<sup>42</sup>, are identified for the pure HZSM-5 zeolite (Fig 13 a). Over the uncalcined Ni/HZSM-5(4) (Fig. 13 b), the peak at *ca.* 1450  $\text{cm}^{-1}$  increases slightly in intensity and that at *ca.* 1540  $\text{cm}^{-1}$  disappears, indicating the “diminishing” of Brönsted acid sites and a bit increase in the concentration of Lewis acid sites, relative to the pure HZSM-5. Over the calcined Ni/HZSM-5(4) (Fig. 13 c), the peak at *ca.* 1450  $\text{cm}^{-1}$  increases obviously in intensity and that at *ca.* 1540  $\text{cm}^{-1}$  appears but with a very small intensity, compared to the uncalcined Ni/HZSM-5(4). This result indicates that, after calcination, the concentration of Lewis acid sites increases and the Brönsted acid sites is, to very small extent, recovered. As has been identified above, both the nickel hydroxide and 1:1 nickel phyllosilicate are present over the uncalcined Ni/HZSM-5(4) (Fig. 2 and Fig. 11), and mainly 2:1 nickel phyllosilicate and a small amount of NiO over the calcined Ni/HZSM-5(4) (Figs. 3 ~ 6 and 9 ~ 12). The increase in the Lewis acidity over the Ni/HZSM-5(4) can be ascribed to the presence of nickel species. It was reported that, Lewis acid sites are generated on the nickel ion-exchanged zeolite or nickel oxides, due to the presences of the unsaturated nickel cations<sup>73, 79-81</sup>, which can absorb pyridine molecules

coordinately as electron-acceptors<sup>73, 79</sup>. In addition, the 1:1 and 2:1 nickel phyllosilicates as well as nickel hydroxide all possess a lamellar structure<sup>31</sup>. The 1:1 nickel phyllosilicate consists of a brucite-type sheet containing Ni(II) in octahedral coordination and a sheet containing linked tetrahedral SiO<sub>4</sub> units, and the 2:1 nickel phyllosilicate comprises two sheets of linked SiO<sub>4</sub> units sandwiching a brucite-type octahedral-coordinated Ni(II) sheet. The layers of 1:1 nickel phyllosilicate are neutral, exhibiting no ion-exchange property, while those in the 2:1 nickel phyllosilicate can be negatively charged, due to the presence of octahedral cation vacancies, when it is low-crystallized, and the electric charges are balanced by the presence of cations in the interlayers. Nickel hydroxides consist of brucitic layers of octahedral Ni(II) with structural OH groups. Depending on the layer stacking, two types of structures may be formed: 1)  $\beta$ -Ni(OH)<sub>2</sub> exhibits a tridimensional structure consisting of stacked brucitic-like layers; 2)  $\alpha$ -Ni(OH)<sub>2</sub> exhibits a bidimensional structure because of the disordered stacking of the nonstoichiometric brucitic layers (Ni(OH)<sub>2-x</sub>), which are separated by intercalated anionic species. The above structural characteristics decide that a Lewis acidity would be present in both the 2:1 nickel phyllosilicate and  $\alpha$ -Ni(OH)<sub>2</sub>, but not in both the 1:1 nickel phyllosilicate and  $\beta$ -Ni(OH)<sub>2</sub>. Therefore, over the uncalcined Ni/HZSM-5(4), the presences of nickel species, such as, a small amount of nickel ions due to ion-exchange and / or deposited  $\alpha$ -Ni(OH)<sub>2</sub>, may

account for the slightly increased in the Lewis acidity, compared to the pure HZSM-5. Over the calcined Ni/HZSM-5, the 2:1 nickel phyllosilicate as the prominent nickel species, generated *via* the transformation of 1:1 nickel phyllosilicate, and also, the NiO, due to the decomposition of nickel hydroxides, would contribute the larger Lewis acidity than over the uncalcined Ni/HZSM-5(4). The disappearance of Brønsted acidity over the uncalcined Ni/HZSM-5 can be due to the blockage of pores in the ZSM-5 zeolite by deposited nickel hydroxides, inhibiting the adsorption of pyridine molecules on the bridged (SiOHAl) hydroxyl groups. The calcination leads to the decomposition of nickel hydroxides into NiO and formation of nickel phyllosilicates, and thus, enables a proportion of bridged (SiOHAl) hydroxyl groups, mainly those located near the outer surface of ZSM-5 zeolite, to be accessible to the adsorption of pyridine molecules, recovering partially the Brønsted acidity.

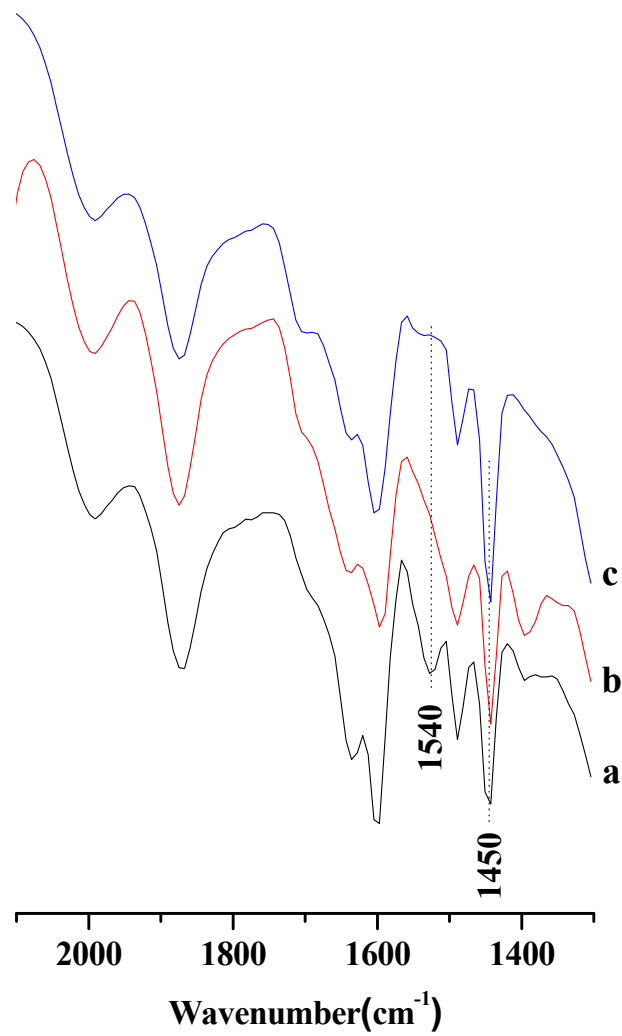
**Figure 13**

Fig. 13 FT-IR spectra for pyridine adsorption over (a) HZSM-5, (b) uncalcined Ni/HZSM-5(4) and (c) calcined Ni/HZSM-5(4).

Fig. 14 shows the pyridine adsorption FT-IR spectra in the 2200 ~ 1200  $\text{cm}^{-1}$  region over the pure HZSM-5 and calcined Ni/HZSM-5(X) (X = 1 ~ 24 h). One can see that, with increasing the D-P time, the band at *ca.* 1450  $\text{cm}^{-1}$  increases slightly in intensity, particularly for a relatively short D-P time. This is due to the fact that, with increasing the D-P time, more nickel species are deposited in the form of nickel hydroxide, and after calcination, they are transformed into NiO and 1:1 or 2:1 nickel phyllosilicates, increasing the concentration of Lewis acid sites. However, with increasing the D-P time, the band at *ca.* 1540  $\text{cm}^{-1}$  remains almost unchanged, indicating that the concentration of Brønsted acid sites is almost unaffected by the D-P time. This finding confirms the deduction made from Fig. 12 that the interaction between nickel species and bridged (SiOHAl) hydroxyl groups is weak.

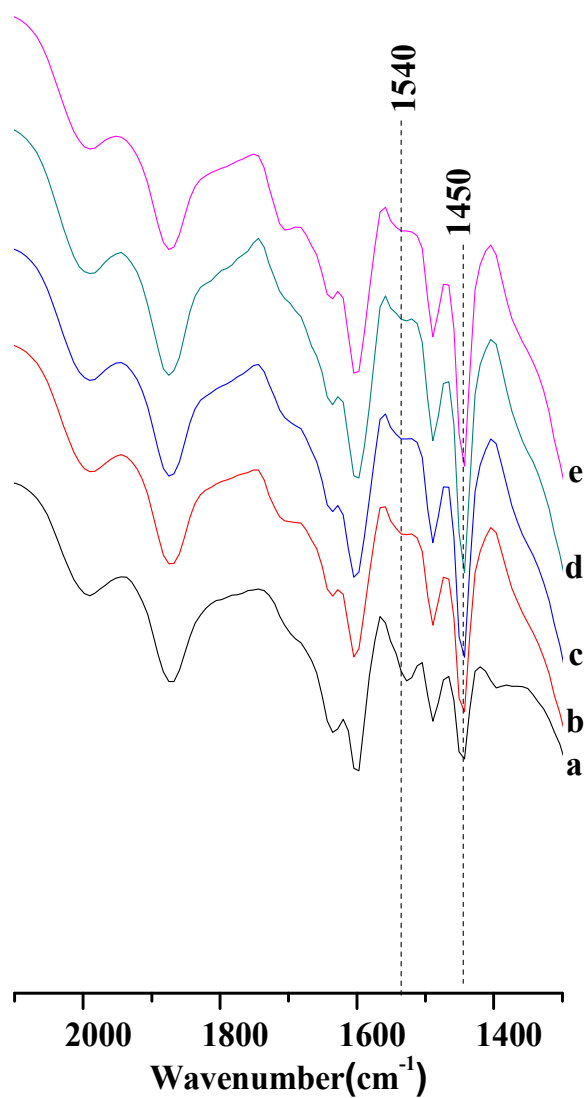
**Figure 14**

Fig. 14 FT-IR spectra for pyridine adsorption over HZSM-5 and Ni/HZSM-5(X) prepared at various D-P time; (a) HZSM-5; (b) ~ (e), Ni/HZSM-5(X) with D-P time X= 1, 2, 4, 8 and 24 h, respectively.

Fig. 15 shows the  $^{27}\text{Al}$  MAS NMR spectra over the calcined Ni/HZSM-5(X) (X = 1 ~ 24 h). One can see that a strong peak at  $\delta = 52$  ppm, being ascribed to the typical four-coordinated framework aluminum in ZSM-5 zeolite <sup>44</sup>, and a very weak peak at  $\delta = 52$  ppm, being attributed to the octahedral non-framework aluminum, are present over all the Ni/HZSM-5(X). Both the intensity and position of the two peaks are found to be almost unchanged with the D-P time. The amount of non-framework aluminum is calculated to account for no more than 2 % of that of total Al atoms for all the Ni/HZSM-5(X) catalysts; thus, they may be neglected, relative to the framework aluminum. The above results indicate that, there is a weak interaction between nickel species and bridged (SiOHAl) hydroxyl groups, and the dealumination of zeolite framework during the D-P process is very little.

Figure 15

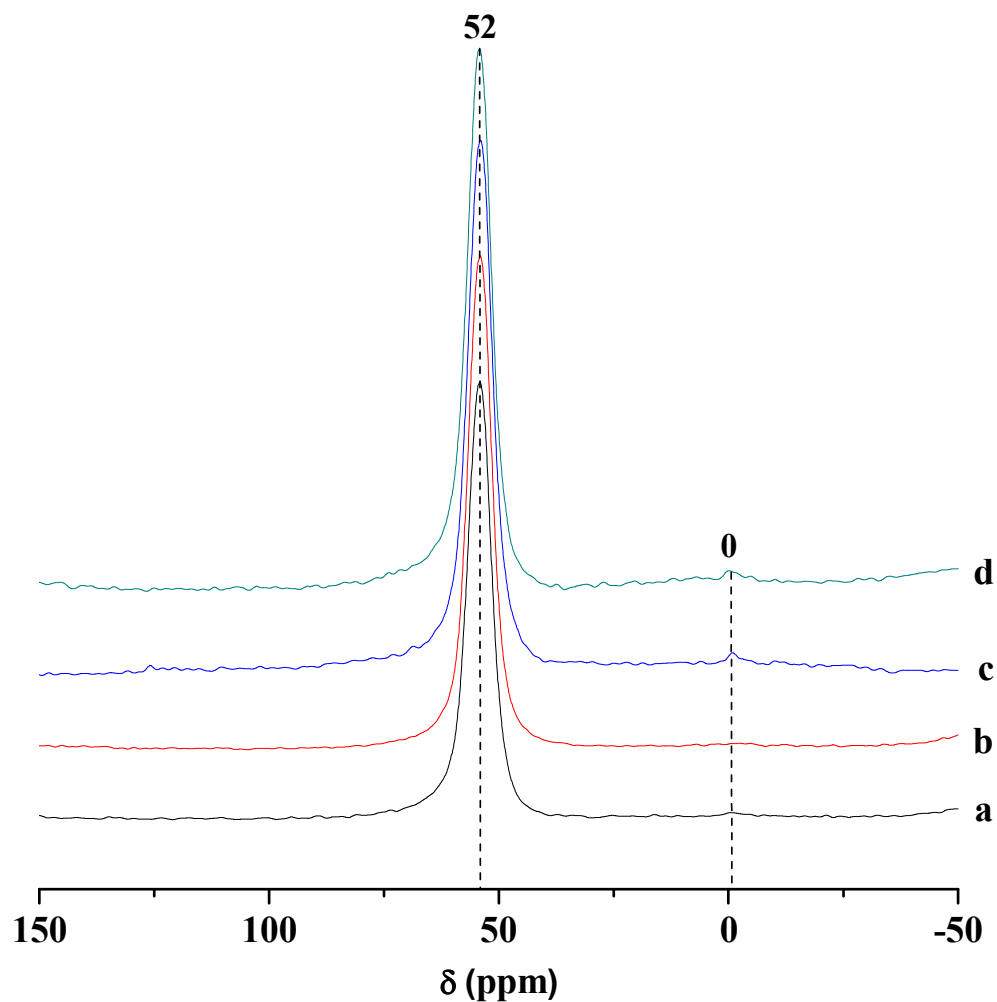
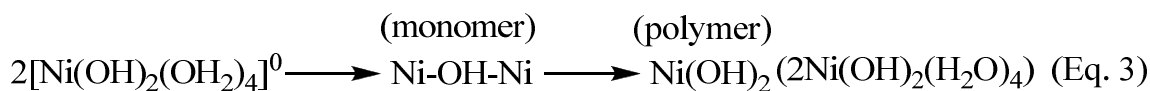
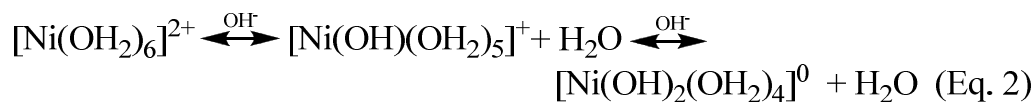


Fig. 15  $^{27}\text{Al}$  MAS NMR spectra over Ni/HZSM-5(X) prepared at various D-P time; (a) ~ (d), D-P time X = 1, 4, 12 and 24 h, respectively.

### 3.2 On the formation of deposit-precipitated nickel(II) phases

It is known that  $[\text{Ni}(\text{OH}_2)_6]^{2+}$  species does not show an acidic behavior, and thus, its hydrolysis to nickel hydroxides precipitate requires the addition of alkaline.

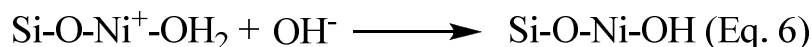
According to Burattin *et al.*<sup>33</sup>, two types of hydroxo-aqua nickel(II) complexes, *i.e.*,  $[\text{Ni}(\text{OH})(\text{OH}_2)_5]^+$  and  $[\text{Ni}(\text{OH})_2(\text{OH}_2)_4]^0$ , were first generated (Eq. 2), and then, the latter as zero-charged precursor condensed infinitely through an olation-type reaction to form a solid phase, and finally generated nickel hydroxides (Eq. 3).



A few papers dealt with the preparation of nickel phyllosilicates; however, the related mechanism is still in debate. Up till now, mainly three kinds of mechanisms have been proposed. In the first kind of mechanism, Mizutani *et al.*<sup>82</sup> proposed, basing on the reaction of nickel chloride and silicic acid in aqueous solution, that aqua-nickel cation was first deprotonated by  $\text{OH}^-$  (Eq. 4), due to its larger acidity than silicic acid, and then subjected to a condensation reaction with silicic acid to generate the intermediate *I* of 1:1 nickel phyllosilicate (Eq. 5):



After that, in the presence of excess silicic acid, the further condensation reaction of intermediate *I* with silicic acid occurred upon the addition of OH<sup>-</sup>, generating the intermediate *II* of 2:1 nickel phyllosilicate (Eqs. 6 and 7):



This mechanism was supported by the fact that the crystal structure of nickel phyllosilicates could be accurately controlled by the Ni/Si molar ratios in the starting mixture to generate the 1:1 and 2:1 nickel phyllosilicates. However, a few arguments were present against this mechanism. For examples, Burattin *et al.*<sup>33</sup> pointed out that the formations of monomers *I* and *II* were lack in experimental proof and the subsequent polymerizations of monomers to phyllosilicates were not described in the literature; Mizutani *et al.*<sup>82-85</sup> claimed that nickel aqua complex might be not more acidic than silicic acid, since the hydrolysis constant pK<sub>1</sub> of Si(OH)<sub>4</sub> could vary between 8 and 10 and that of Ni(H<sub>2</sub>O)<sub>6</sub> between 6.5 and 10.9, dependent on the ionic strength and temperature of solution.

The second kind of mechanism was proposed by Henry, *et al.*<sup>33</sup>, basing on the assumption that the proton of Si(OH)<sub>4</sub> was preferentially ionized before the deprotonation of aqua nickel cation (see Eq. 4), as shown by Eqs. 8 and 9:



Since  $[\text{SiO(OH)}_3]^-$  possessed larger nucleophilicity than  $[\text{Ni(OH)(H}_2\text{O)}_5]^+$  or  $[\text{Ni(OH)}_2(\text{H}_2\text{O)}_4]^0$ , its condensation with  $[\text{Ni(H}_2\text{O)}_6]^{2+}$  to generate nickel phyllosilicates was kinetically faster than the formation of nickel hydroxides *via* the condensation reactions described by Eqs. 2 and 3. This mechanism was employed to explain the observation that the entities of nickel phyllosilicates had been detected within the first seconds of preparation.

Burattin *et al.*<sup>31, 33</sup> studied the deposition-precipitation of nickel(II) species over silica and proposed the third kind of mechanism<sup>33</sup>. The authors found that nickel hydroxide and 1:1 nickel phyllosilicate was generated respectively over silica with low and high surface area for short D-P time ( $\leq 4$  h), and 1:1 nickel phyllosilicate was formed independent on the surface area of silica for long D-P time ( $> 4$  h)<sup>31</sup>. It was therefore suggested that Ni(II) hexa aqua complexes were in equilibrium with  $[\text{Ni(OH)(OH}_2)_5]^+$  and  $\text{Ni(OH)}_2(\text{OH}_2)_4$ . The zero-charged precursors  $\text{Ni(OH)}_2(\text{OH}_2)_4$  can be first reacted with the silanol groups of silica support *via* an hydrolytic adsorption (Eq. 10), and then subjected to an olation-type hetero-condensation reaction. It is also possible that the precursors  $\text{Ni(OH)}_2(\text{OH}_2)_4$  react first with each other in the solution phase and then with the

silica support. Both the above two processes generate a brucitic layer of octahedral Ni(II) bonded to the silica surface, which is in fact a sheet of 1:1 nickel phyllosilicate at the support-solution interface.



Meanwhile,  $\text{Si}(\text{OH})_4$  is generated and released into solution due to the dissolution of silica. In the case that silica with high surface area is involved, an enough high amount of  $\text{Si}(\text{OH})_4$  is available, due to the large support-solution interface, for the hetero-condensation reaction with nickel complexes in solution to generate the Si-O-Ni monomers, and the further polymerization leads to the formation of 1:1 nickel phyllosilicate on the above mentioned brucitic layer. However, in the case that silica with low surface area is involved, the amount of  $\text{Si}(\text{OH})_4$  released is insufficient, particularly for short D-P time, due to the small support-solution interface, and thus, the Si-O-Ni hetero-condensation is a minor reaction and the olation between  $\text{Ni}(\text{OH})_2(\text{OH}_2)_4$  complexes a main one, leading to the formation of supported nickel hydroxide. The generation of 1:1 nickel phyllosilicate from the Ni-O-Si hetero-condensation/polymerization is faster, however, being limited by both the concentration of silicic acid dissolved in solution and its diffusion rate, than that of nickel hydroxide from the Ni-OH-Ni olation/polymerization, while the formation of nickel hydroxide ( $\Delta G_f^\circ = -1870$

Kcal/mol) is more favorable in thermodynamics than that of 1:1 nickel phyllosilicate ( $\Delta G_f^\circ = -690$  Kcal/mol)<sup>33</sup>. Thus, the whole mechanism is governed by kinetics and not by thermodynamics. It should be noted that, in Burattin's work<sup>31,33</sup>, no 2:1 nickel phyllosilicate was identified even for a D-P time longer than 16 h, although the 2:1 nickel phyllosilicate ( $\Delta G_f^\circ = -1040$  Kcal/mol) is more stable thermodynamically than the 1:1 nickel phyllosilicate ( $\Delta G_f^\circ = -690$  Kcal/mol)<sup>33</sup>. As pointed by the authors, the 2:1 nickel phyllosilicate could be only observed *via* the further hydrothermal treatment of 1:1 nickel phyllosilicate at 190 °C for 7 days, involving the depolymerization of 1:1 nickel phyllosilicate formed first and re-precipitation of 2:1 nickel phyllosilicate. No matter whichever mechanism mentioned above is involved in the generation of nickel phyllosilicates, a prerequisite should be fulfilled, *i.e.*, the silicic species in solution must be monomeric before the generation of nickel phyllosilicates. This fact indicates that the generation of nickel phyllosilicates is largely limited to the concentration of monomeric silicic species.

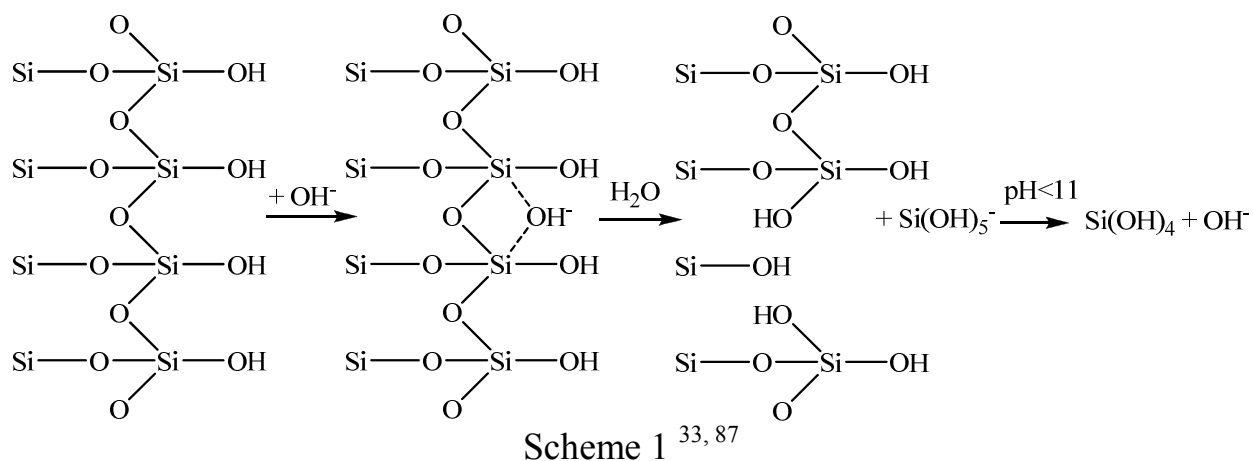
In our work, as has been obtained in section 3.1, it is identified that the D-P of nickel species on HZSM-5 consists of two stages, *i.e.*, the deposition of nickel species and their aging. In the first stage (D-P time < 2 h), nickel hydroxides are first deposited over the zeolite and then gradually transformed into the ill-crystalline 1:1 nickel phyllosilicate (2 h < D-P time < 4 h). In the second stage ( $\geq$

4 h), the crystalline 1:1 nickel phyllosilicate is generated from the ill-crystalline nickel phyllosilicate. The calcination leads to the generation of 1:1 nickel phyllosilicate from the transformation of nickel hydroxide, and that of 2:1 nickel phyllosilicate from the transformation of 1:1 nickel phyllosilicate. These observations hint that the mechanism for the D-P of nickel species over HZSM-5 is different from all the above reported in the literature. It is suggested that not only dynamics but also thermodynamics control the D-P process of nickel over HZSM-5 zeolite. In considering that siliceous ZSM-5 zeolite can be hydrothermally synthesized from silica in strong alkaline solution, and also, crystalline ZSM-5 zeolite is more stable than amorphous silica, the dissolution rate of silicon for ZSM-5 zeolite in the weak basic solution of urea (at heating) should be much lower than that for silica. This decides that the concentration of monomeric silicic species dissolved in solution is very limited. Thus, for a short D-P time ( $< 2$  h), the nickel hydroxide, being also more thermodynamically stable than nickel phyllosilicates, is predominantly generated and deposited over the HZSM-5 zeolite, through the similar Ni-OH-Ni olation/polymerization reaction as mentioned in the above Burattin's mechanism. With increasing the D-P time ( $2 \text{ h} < \text{D-P time} \leq 4 \text{ h}$ ), the amount of monomeric silicic species, generated *via* the dissolution of ZSM-5 zeolite framework, increases. Because the Ni-O-Si heterocondensation/polymerization is faster than the Ni-OH-Ni olation/polymerization,

as pointed in the above Burattin's mechanism, both the 1:1 nickel phyllosilicate and nickel hydroxide can be generated over the ZSM-5 zeolite support. Meanwhile, a proportion of monomeric silicic species can be also adsorbed over the ZSM-5 zeolite due to its high surface area and porosity. With increasing further the D-P time ( $> 4$  h), the nickel species are completely consumed in generating the 1:1 nickel phyllosilicate, and thus, the monomeric silicic species are only adsorbed over the ZSM-5 zeolite. After calcination, the dehydration between the Si-OH groups and deposited nickel hydroxide leads to the generation of 1:1 nickel phyllosilicate, and that between the adsorbed monomeric silicic species and Ni-OH groups in the 1:1 nickel phyllosilicate results in the formation of 2:1 nickel phyllosilicate.

### 3.3 On the role of hydroxyl groups

It was reported that there are abundant amounts of structural defect sites and thus internal Si-OH groups in highly siliceous ZSM-5 zeolite<sup>4,24</sup>. The framework of ZSM-5 zeolite can be partially dissolved in a basic solution to release monomeric silicic species in solution, and the related mechanism probably obeys the similar pathway as that of silicas<sup>33,86</sup>, which is depicted as follows (scheme 1):



One can see that  $\text{OH}^-$  ions are first adsorbed close to the Si-OH sites on the ZSM-5 zeolite, and then, the S-O-Si bonds in the Si-OH sites are broken, releasing the dissolved monomeric silicic species into the solution. It is obvious that the dissolution of silicon is largely dependent on the concentration of Si-OH groups over zeolite <sup>87</sup>. Cizmek *et al.* <sup>86</sup> investigated the dissolution of “as-synthesized” (pristine, without removing the template agents) and “activated” (organic-free) highly siliceous ZSM-5 zeolites in heated NaOH solution, and it was found that the dissolution rate of “activated” zeolites was six-folds higher than their “as-synthesized” homologues. This phenomenon illuminates that the dissolution of highly siliceous zeolites occurs mainly over the internal surface rather than the external surface, due to the high internal specific surface area and abundant internal silanol groups.

In our work, as has been obtained in section 3.1, it is identified (see Fig. 11 and 12) that, after a 1 h of D-P, the 1:1 nickel phyllosilicate is generated, accompanied

with the decreases in both the concentrations of “hydroxyls nests” and clusters of internal Si-OH groups involved in the delocalized hydrogen-bonded linear and ring chains, while the concentration of isolated Si-OH groups located at internal sites remains almost unchanged. The increase in the D-P time within 4 h leads to the formation of more 1:1 nickel phyllosilicate, with the concentration of the clusters of internal Si-OH groups involved in the delocalized hydrogen-bonded linear and ring chains being decreased largely and those of “hydroxyls nests” and isolated Si-OH groups located at internal sites remaining stable. The further increase in the D-P time beyond 4 h consumes completely the internal Si-OH groups involved in the delocalized hydrogen-bonded linear and ring chains, leaving the “hydroxyls nests” and isolated Si-OH groups unchanged. The above results suggest that, the interaction between nickel species and internal Si-OH groups involved in the delocalized hydrogen-bonded linear and ring chains, which locate in the mesopores or nanocavities generated *via* the aggregations of “hydroxyls nests”, contributes predominantly to the formation of 1:1 nickel phyllosilicate, and that between nickel species and single “hydroxyls nest” contributes relatively less, but the isolated internal Si-OH groups almost does not take part in the formation of 1:1 nickel phyllosilicate. It seems that the accessibility of internal Si-OH groups, *i.e.*, steric effect, affects significantly the formation of 1:1 nickel phyllosilicates. In fact, as pointed out in the Burattin’s mechanism (see section 3.2), the 1:1 nickel

phyllosilicate is formed due to either the first deposition of nickel hydroxide on the Si-OH groups of ZSM-5 support, through the Ni-OH-Ni oligation/polymerization reaction and subsequent dehydration between the Ni-OH and Si-OH groups, or the direct Ni-O-Si hetero-condensation/polymerization. Therefore, the larger the accessibility of Si-OH is, the easier is both the deposition of nickel hydroxide and its transformation into the 1:1 nickel phyllosilicate to occur. As depicted in scheme 1, the dissolution of ZSM-5 zeolite framework to generate the silicic species in solution occurs at the locations close to the adjacent Si-OH groups, and therefore, the internal Si-OH groups involved in the delocalized hydrogen-bonded linear and ring chains are more easily to be dissolved, due to their large accessibility, than the other internal Si-OH groups, *e.g.*, “hydroxyls nests” and isolated internal silanols.

The results in section 3.1 show also that both the external terminal Si-OH and bridged (Si-OH-Al) hydroxyl groups have almost no change during the D-P process, contributing very little to the deposition of nickel hydroxide and generation of nickel phyllosilicate during the D-P process (see Figs. 11 ~ 15). This occurs most probably due to the fact that, the external terminal Si-OH groups have a very small amount, accounting for only a very small proportion of total silanols in highly siliceous ZSM-5 zeolite, to say nothing of external surficial bridged (Si-OH-Al) hydroxyl groups, of which the total amount is significantly smaller than

silanols. As mentioned in the Burattin's mechanism, the deposition of nickel hydroxide involves the hydrolytic adsorption of Ni(II) complex over the silanol groups over silica support and subsequent Ni-OH-Ni ololation/polymerization; both of the two processes are unfavorable in the case that the separated and very small amount of external terminal Si-OH groups are involved. In addition, the generation of silicic species released in solution involves the attacking of OH<sup>-</sup> on silicon atom with adjacent Si-OH groups (see scheme 1). Thus, the lack in adjacent Si-OH groups for both the external terminal Si-OH and bridged (Si-OH-Al) hydroxyl groups therefore enables them to be almost intact during the D-P process.

### **3.4 Proposed mechanism for deposition-precipitation (D-P) of Ni (II) species over highly siliceous HZSM-5 zeolite**

Basing on the above discussions on the role of hydroxyl groups and formation of deposit-precipitated Ni(II) species, a mechanism for the D-P of Ni(II) species over highly siliceous HZSM-5 zeolite has been proposed, as illustrated in Fig. 16. It has been reported in volumes of literature that not only nickel hydroxides but also nickel phyllosilicates are generated over silica-containing supports during the D-P process. The generation of nickel phyllosilicates is a result of the interaction between aqua nickel ions and dissolved monomer silicic species, while the deposition of nickel hydroxides involves their interaction with silanol groups. When the support is the highly siliceous HZSM-5, the above processes involve

mainly the silanol groups in the internal hydroxylated mesopores or nanocavities, of which the structure is shown in the left-upper of Fig. 16. At the beginning of D-P process, aqua  $[\text{Ni}(\text{OH}_2)_6]^{2+}$  species are hydrolyzed (step 1 a), in the presence of hydroxide ions released from urea precipitant, into  $[\text{Ni}(\text{OH})(\text{OH}_2)_5]^+$  and/or  $[\text{Ni}(\text{OH})_2(\text{OH}_2)_4]^0$  hydroxo aqua nickel(II) complexes (step 1 b). The oligation condensation of  $[\text{Ni}(\text{OH})_2(\text{OH}_2)_4]^0$  results in the Ni-OH-Ni monomer (step 1 c), and the infinite polymerization of the latter generates nickel hydroxides over HZSM-5 zeolite (step 1 d), due to their interaction with internal silanol groups. With the progress of D-P process, monomer silicic species are also generated in solution due to the partial dissolution of HZSM-5 zeolite framework (Step 2 a ~ c). The monomer silicic species can be either re-adsorbed over HZSM-5 zeolite (step 2 d) or subjected to the hetero-condensation with the  $[\text{Ni}(\text{OH})(\text{OH}_2)_5]^+$ , resulting in Si-O-Ni monomer (step 3 a). After the polymerization of Si-O-Ni monomer, 1:1 nickel phyllosilicate is generated over the HZSM-5 zeolite (step 3 b). The 1:1 nickel phyllosilicate can be also formed *via* the hydrolytic adsorption of  $[\text{Ni}(\text{OH})(\text{OH}_2)_5]^+$  and/or  $[\text{Ni}(\text{OH})_2(\text{OH}_2)_4]^0$  hydroxo aqua nickel(II) complexes over adjacent silanol groups (step 4 a) and their subsequent oligation condensation (step 4 b). During the calcination, the deposited nickel hydroxide is transformed into nickel oxide, while the 1:1 nickel phyllosilicate is reacted with the adsorbed monomer silicic species to generate the 2:1 nickel phyllosilicate (step 5). The

above processes are more concisely shown by the schematic diagram in the lower region of Fig. 16. According to the above mechanism, over the calcined Ni/HZSM-5 catalyst, Ni(II) species are present in both the form of nickel oxide and 2:1 phyllosilicate, which are mutually separated each other, being highly dispersed over HZSM-5 zeolite.

Figure 16

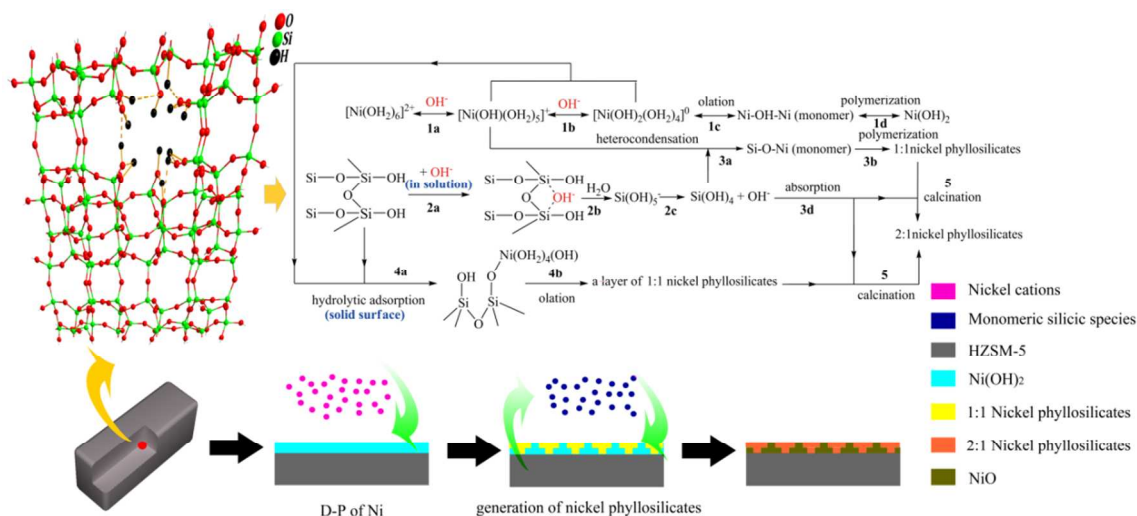


Fig. 16 Proposed mechanisms for the deposition-precipitation (D-P) of Ni(II) species on highly siliceous HZSM-5 zeolite

## 5. Conclusion

Basing on the identifications of hydroxyl groups and deposit-precipitated Ni(II) species, a mechanism for the D-P of Ni(II) species over highly siliceous HZSM-5 zeolite, involving the competition between the generation of nickel hydroxides and that of nickel phyllosilicates, has been proposed. This mechanism is different from that for the D-P of nickel(II) species over silica reported in the literature, because of the larger specific surface area and lower dissolution rate of

silicon for the highly siliceous HZSM-5 zeolite than for the silica. The main points of the proposed mechanism are as follows:

- 1) The D-P of nickel species occurs predominantly on the internal silanol groups located at the hydroxylated mesopores or nanocavities in the HZSM-5 zeolite, because of the large accessibility of these silanol groups, relative to other kinds of silanol groups;
- 2) During the D-P process, nickel hydroxide is first deposited-precipitated *via* olation/polymerization of neutral hydroxo aqua nickel species over the HZSM-5 zeolite, due to the limited concentration of dissolved monomer silicic species;
- 3) With the progress of D-P process, 1:1 nickel phyllosilicate is formed over the HZSM-5 *via* the hetero-condensation/polymerization between charged hydroxo aqua nickel species and dissolved monomer silicic species. Alternatively, the 1:1 nickel phyllosilicate can be generated *via* the hydrolytic adsorption of hydroxo aqua nickel species over adjacent silanol groups and their subsequent olation condensation.
- 4) After calcination, the deposited-precipitated nickel hydroxide is decomposed into nickel oxide, while the 1:1 nickel phyllosilicate is transformed into 2:1 nickel phyllosilicate.

According to the above mechanism, both the nickel oxide and 2:1 phyllosilicate, which are mutually separated each other, are generated *via* the D-P process, being beneficial to the high dispersion of nickel over highly siliceous HZSM-5 zeolite.

## Acknowledgment

We are grateful to the financial supports from the Project #21376068 for National Natural Science Foundation (NSFC), Program for Lotus Scholar in Hunan Province, and also, Program for Innovative Research Team (Hunan University: IRT1238) of MOE, China.

## References

1. D. W. Breck, *Zeolite molecular sieves: structure, chemistry, and use*, Wiley New York, 1973.
2. S. Bhatia, *Zeolite catalysts: principles and applications*, CRC press, 1989.
3. R. T. Yang, A. J. Hernandez-Maldonado and F. H. Yang, *Science*, 2003, **301**, 79-81.
4. K. Yamagishi, S. Namba and T. Yashima, *J. Phys. Chem.*, 1991, **95**, 872-877.
5. B.-H. Chen, C. Huang, D.-G. Huang, C.-W. Luo, H.-T. Li and Z.-S. Chao, *Appl. Catal. A: Gen.*, 2014, **470**, 239-249.
6. P. Wu, T. Komatsu and T. Yashima, *J. Phys. Chem.*, 1995, **99**, 10923-10931.
7. D. F. Shantz, J. Schmedt auf der Günne, H. Koller and R. F. Lobo, *J. Am. Chem. Soc.*, 2000, **122**, 6659-6663.
8. S. Bordiga, I. Roggero, P. Ugliengo, A. Zecchina, V. Bolis, G. Artioli, R. Buzzoni, G. Marra, F. Rivetti, G. Spano and C. Lamberti, *J. Chem. Soc., Dalton Trans.*, 2000, 3921-3929.
9. S. Bordiga, P. Ugliengo, A. Damin, C. Lamberti, G. Spoto, A. Zecchina, G. Spanò, R. Buzzoni, L. Dalloro and F. Rivetti, *Top. Catal.*, 2001, **15**, 43-52.
10. G. Artioli, C. Lamberti and G. Marra, *Acta Cryst. B*, 2000, **56**, 2-10.
11. A. Zecchina, S. Bordiga, G. Spoto, L. Marchese, G. Petrini, G. Leofanti and M. Padovan, *J. Phys. Chem.*, 1992, **96**, 4985-4990.
12. F. Mizukami, *Stud. surf. sci. catal.*, 1999, **125**, 1-12.
13. S. W. Blocki, *Environ. Prog.*, 1993, **12**, 226-230.
14. H. Pande and P. Parikh, *J. Mater. Eng. Perf.*, 2013, **22**, 190-199.
15. X. Zhu, S. Liu, Y. Song and L. Xu, *Appl. Catal. A: Gen.*, 2005, **288**, 134-142.
16. Y.-c. Long, H.-w. Jiang and H. Zeng, *Langmuir*, 1997, **13**, 4094-4101.
17. R. R. Mukti, H. Hirahara, A. Sugawara, A. Shimojima and T. Okubo, *Langmuir*, 2009, **26**, 2731-2735.
18. B. Sulikowski, J. Datka, B. Gil, J. Ptaszynski and J. Klinowski, *J. Phys. Chem. B*, 1997, **101**, 6929-6932.
19. R. Borade, A. Sayari, A. Adnot and S. Kaliaguine, *J. Phys. Chem.*, 1990, **94**, 5989-5994.
20. Y. Tang, B. Li, N. Zhang, S. Wang, Y. Wen, P. Jin and X. Wang, *CrystEngComm*, 2012, **14**, 3854-3857.
21. Q. Yu, Q. Zhang, J. Liu, C. Li and Q. Cui, *CrystEngComm*, 2013, **15**, 7680-7687.
22. A. Masalska, *Appl. Catal. A: Gen.*, 2005, **294**, 260-272.
23. P. Treesukol, K. Srisuk, J. Limtrakul and T. N. Truong, *J. Phys. Chem. B*, 2005, **109**, 11940-11945.
24. M. Hunger, J. Karger, H. Pfeifer, J. Caro, B. Zibrowius, M. Bulow and R. Mostowicz, *J. Chem. Soc., Faraday Trans.*, 1987, **83**, 3459-3468.
25. A. Sokol, C. Catlow, J. Garces and A. Kuperman, *J. Phys. Condens. Matter.*, 2004, **16**, S2781.
26. V. R. R. Marthala, Y. Jiang, J. Huang, W. Wang, R. Gläser and M. Hunger, *J. Am. Chem. Soc.*, 2006, **128**, 14812-14813.
27. B. I. Mosqueda-Jiménez, A. Jentys, K. Seshan and J. A. Lercher, *App. Catal. B: Environ.*, 2003, **43**, 105-115.
28. J. A. Rossin, C. Saldarriaga and M. E. Davis, *Zeolites*, 1987, **7**, 295-300.

29. R. Nares, J. Ramírez, A. Gutiérrez-Alejandre, C. Louis and T. Klimova, *J. Phys. Chem. B*, 2002, **106**, 13287-13293.
30. A. Clearfield, *Chem. Rev.*, 1988, **88**, 125-148.
31. P. Burattin, M. Che and C. Louis, *J. Phys. Chem. B*, 1997, **101**, 7060-7074.
32. M. Kermarec, J. Y. Carriat, P. Burattin, M. Che and A. Decarreau, *J. Phys. Chem.*, 1994, **98**, 12008-12017.
33. P. Burattin, M. Che and C. Louis, *J. Phys. Chem. B*, 1998, **102**, 2722-2732.
34. H. Liu, H. Wang, J. Shen, Y. Sun and Z. Liu, *Appl. Catal. A: Gen.*, 2008, **337**, 138-147.
35. R. n. Nares, J. Ramírez, A. d. Gutiérrez-Alejandre and R. Cuevas, *Ind. Eng. Chem. Res.*, 2008, **48**, 1154-1162.
36. J. W. E. Coenen, *Appl. Catal.*, 1989, **54**, 59-63.
37. D. Costa, G. Martra, M. Che, L. Manceron and M. Kermarec, *J. Am. Chem. Soc.*, 2002, **124**, 7210-7217.
38. F. Ernst, *Mater. Sci. Eng. R*, 1995, **14**, 97-156.
39. J. M. De Teresa, A. Barthelemy, A. Fert, J. P. Contour, F. Montaigne and P. Seneor, *Science*, 1999, **286**, 507-509.
40. M. Stengel, D. Vanderbilt and N. A. Spaldin, *Nat. Mater.*, 2009, **8**, 392-397.
41. A. Zecchina, S. Bordiga, G. Spoto, L. Marchese, G. Petrini, G. Leofanti and M. Padovan, *J. Phys. Chem.*, 1992, **96**, 4991-4997.
42. G. L. Woolery, G. H. Kuehl, H. C. Timken, A. W. Chester and J. C. Vartuli, *Zeolites*, 1997, **19**, 288-296.
43. F. Jin, Y. Cui and Y. Li, *Appl. Catal. A: Gen.*, 2008, **350**, 71-78.
44. W. Zhang, D. Ma, X. Han, X. Liu, X. Bao, X. Guo and X. Wang, *J. Catal.*, 1999, **188**, 393-402.
45. S.-J. Jong and S. Cheng, *Appl. Catal. A: Gen.*, 1995, **126**, 51-66.
46. B. J. Reddy, R. L. Frost and M. J. Dickfos, *Spectrochimica Acta A*, 2009, **71**, 1762-1768.
47. A. Manceau and G. Calas, *Clay Miner.*, 1987, **22**, 357-362.
48. J. T. Klopogge, *J. Porous Mater.*, 1998, **5**, 5-41.
49. F. Basile, G. Fornasari, M. Gazzano and A. Vaccari, *Appl. Clay Sci.*, 2000, **16**, 185-200.
50. L. Bonneviot, O. Legendre, M. Kermarec, D. Olivier and M. Che, *J. Collo. Interf. Sci.*, 1990, **134**, 534-547.
51. F. Prinetto, D. Tichit, R. Teissier and B. Coq, *Catal. Today*, 2000, **55**, 103-116.
52. R. Prihod'ko, E. J. M. Hensen, M. Sychev, I. Stolyarova, T. E. Shubina, I. Astrelin and R. A. van Santen, *Micro. Meso. Mater.*, 2004, **69**, 49-63.
53. A. Davidson, J. F. Tempere, M. Che, H. Roulet and G. Dufour, *J. Phys. Chem.*, 1996, **100**, 4919-4929.
54. E. Ramarosan, J. F. Tempere, M. F. Guilleux, F. Vergand, H. Roulet and G. Dufour, *J. Chem. Soc., Faraday Trans.*, 1992, **88**, 1211-1218.
55. A. Manceau, G. Calas and A. Decarreau, *Clay Miner.*, 1985, **20**, 367-387.
56. R. Newman and R. M. Chrenko, *Phys. Rev.*, 1959, **114**, 1507-1513.
57. W. Mao, H. Ma and B. Wang, *J. Hazard. Mater.*, 2009, **167**, 707-712.
58. L. Kundakovic and M. Flytzani-Stephanopoulos, *Appl. Catal. A: Gen.*, 1998, **171**, 13-29.
59. G. Jacobs, P. M. Patterson, Y. Zhang, T. Das, J. Li and B. H. Davis, *Appl. Catal. A: Gene.*, 2002, **233**, 215-226.
60. A. F. Trasarti, N. M. Bertero, C. R. Apesteguía and A. J. Marchi, *Appl. Catal. A: Gen.*, 2014, **475**, 282-291.

61. A. Gervasini, *Appl. Catal. A: Gen.*, 1999, **180**, 71-82.
62. A. Sommer, G. Fetter, D. Tichit, P. Bosch, E. Palomares and D. Lerner, *Dalton Trans.*, 2014.
63. G. Leofanti, M. Padovan, G. Tozzola and B. Venturelli, *Catal. Today*, 1998, **41**, 207-219.
64. G. Nie, L. Zhang, X. Lu, X. Bian, W. Sun and C. Wang, *Dalton Trans.*, 2013, **42**, 14006-14013.
65. L.-P. Zhu, G.-H. Liao, Y. Yang, H.-M. Xiao, J.-F. Wang and S.-Y. Fu, *Nanoscale res. lett.*, 2009, **4**, 550-557.
66. D. Wang, C. Song, Z. Hu and X. Fu, *J. Phys. Chem. B*, 2005, **109**, 1125-1129.
67. T. Lehmann, T. Wolff, C. Hamel, P. Veit, B. Garke and A. Seidel-Morgenstern, *Micro. Meso. Mater.*, 2012, **151**, 113-125.
68. J. C. Vedrine, G. Hollinger and D. Tran Minh, *J. Phys. Chem.*, 1978, **82**, 1515-1520.
69. G. Wendt, D. Hentschel, J. Finster, R. Schöllner, S. Hanafi and R. S. Mikhail, *J. Chem. Soc., Faraday Trans.*, 1983, **79**, 2013-2025.
70. R. Beyerlein, C. Choi-Feng, J. Hall, B. Huggins and G. Ray, *Top. Catal.*, 1997, **4**, 27-42.
71. F. Jin and Y. Li, *Catal. Today*, 2009, **145**, 101-107.
72. M. Mihaylov and K. Hadjiivanov, *Langmuir*, 2002, **18**, 4376-4383.
73. A. Zecchina, E. Guglielminotti, L. Cerruti and S. Coluccia, *J. Phys. Chem.*, 1972, **76**, 571-577.
74. A. Zecchina, S. Bordiga, G. Spoto, D. Scarano, G. Petrini, G. Leofanti, M. Padovan and C. O. Arean, *J. Chem. Soc., Faraday Trans.*, 1992, **88**, 2959-2969.
75. S. Yang, X. Wu, C. Chen, H. Dong, W. Hu and X. Wang, *Chem. Commun.*, 2012, **48**, 2773-2775.
76. M. B. J. G. Freitas, *J. Power Sources*, 2001, **93**, 163-173.
77. K. Barbera, F. Bonino, S. Bordiga, T. V. W. Janssens and P. Beato, *J. Catal.*, 2011, **280**, 196-205.
78. P. Hoffmann and J. A. Lobo, *Micro. Meso. Mater.*, 2007, **106**, 122-128.
79. J. W. Ward, *J. Catal.*, 1968, **10**, 34-46.
80. M. D. Romero, J. A. Calles and A. Rodríguez, *Ind. Eng. Chem. Res.*, 1997, **36**, 3533-3540.
81. C. Minchev, S. A. Zubkov, V. Valtchev, V. Minkov, N. Micheva and V. Kanazirev, *Appl. Catal. A: Gen.*, 1994, **119**, 195-204.
82. T. Mizutani, Y. Fukushima, A. Okada and O. Kamigaito, *Bull. Chem. Soc. Jpn.*, 1990, **63**, 2094-2098.
83. T. Mizutani, Y. Fukushima and O. Kamigaito, *Bull. Chem. Soc. Jpn.*, 1990, **63**, 618-619.
84. B. CF Jr and R. Mesmer, *The hydrolysis of cations*, John Wiley and Sons, New York, 1976.
85. J. Burgess, *Metal ions in solution*, Ellis Horwood, Chichester, 1978.
86. A. Čimek, B. Subotić, I. Šmit, A. Tonejc, R. Aiello, F. Crea and A. Nastro, *Micro. Mater.*, 1997, **8**, 159-169.
87. R. K. Iler, *The chemistry of silica: Solubility, polymerization, colloid and surface properties, and biochemistry*, Wiley (New York), 1979.

**Table 1 Assignments of the optical transitions of various Ni(II) species**

	Spin-allowed transitions				Spin-forbidden transitions			ref
	${}^3T_{1g}({}^3P)$	${}^3T_{1g}({}^3F)$	${}^3T_{2g}({}^3F)$	${}^1E_g({}^1D)$	${}^1T_{2g}$	${}^1A_{1g}(D)$	${}^1T_{1g}(D)$	
	v1	v2	v3	v2'				
Nepouite <sup>a</sup> (1:1)	384	650	1086	747				46
Ni-Talc <sup>b</sup> (2:1)	388	577 650	1117	736				55
	389	685	1136	755				54
Ni(OH) <sub>2</sub>	385	660	1120	730				55
	386	654	1127	730				53
	408	652	1147	710	456	379	337	53
NiO	418	653	1123	719	458	380	346	47
	420	637	1098	709	450	381	352	56

\* v2' appears as the shoulder of the v2 band; <sup>a</sup> Nepouite is 1:1 nickel phyllosilicate (Si<sub>2</sub>Ni<sub>3</sub>O<sub>5</sub>(OH)<sub>4</sub>); <sup>b</sup> Ni-Talc is 2:1 nickel phyllosilicate (Si<sub>4</sub>Ni<sub>3</sub>O<sub>10</sub>(OH)<sub>2</sub>).

**Table 2 Actual Ni loading, reduction degree of Ni and surface metal density over Ni/HZSM-5(X) prepared at various D-P time**

Catalyst	Reduction degree <sup>a</sup> (%)	Surface metallic density <sup>b</sup> (10 <sup>20</sup> atoms/g catalyst)
Ni/HZSM-5(2)	93	1.3
Ni/HZSM-5(4)	56	1.1
Ni/HZSM-5(12)	27	1.2
Ni/HZSM-5(24)	25	1.7

<sup>a</sup> identified by O<sub>2</sub>-TPO; <sup>b</sup> estimated by H<sub>2</sub>-TPD <sup>31</sup>.

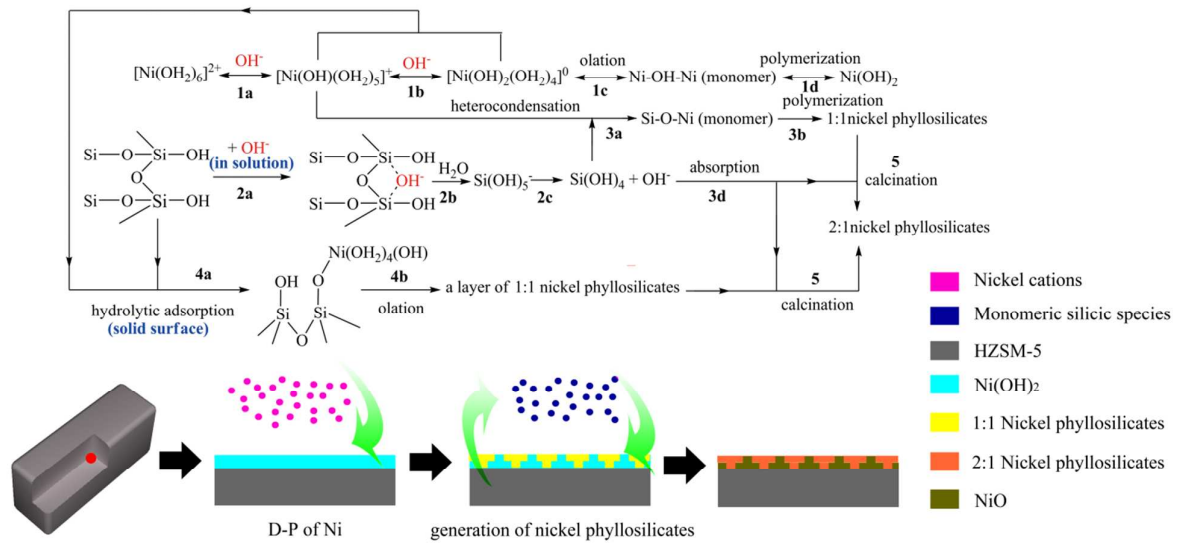
**Table 3 Textural properties for various samples**

Samples	$S_{BET}$ (m <sup>2</sup> /g)	$V_{pore,t}$ (cm <sup>3</sup> /g)	$S_{mic}$ (m <sup>2</sup> /g)	$S_{ext}$ (m <sup>2</sup> /g)	$V_{pore,mic}$ (cm <sup>3</sup> /g)	$V_{pore,mes}$ (cm <sup>3</sup> /g)	$D_{pore,mes}$ (Å)
HZSM-5	374	0.234	289	85	0.133	0.101	/
Ni/HZSM-5(1)	346	0.272	253	93	0.111	0.161	16.7
Ni/HZSM-5(4)	330	0.272	211	119	0.092	0.180	17.0
Ni/HZSM-5(8)	358	0.488	202	156	0.094	0.394	17.8
Ni/HZSM-5(12)	373	0.503	200	173	0.089	0.414	19.0
Ni/HZSM-5(24)	401	0.656	174	228	0.083	0.573	19.5

*Notes:*

- 1) The meanings of symbols in the first row:  $S_{BET}$ , specific surface area;  $S_{mic}$ , micropore area;  $S_{ext}$ , external surface area;  $S_{BET} = S_{mic} + S_{ext}$ ;  $V_{pore,t}$ , total pore volume;  $V_{pore,mic}$ , micropore volume;  $V_{pore,mes}$ , mesoporous volume;  $V_{pore,t} = V_{pore,mes} + V_{pore,mic}$ ;  $D_{pore,mes}$ , average mesopore size calculated by BJH method.
- 2) Because of its microporous characteristic, the pure HZSM-5 is inapplicable in the estimation of average mesopore size by BJH method.

## TOC:



Mechanism for the preparation of highly siliceous HZSM-5 zeolite supported nickel catalysts via deposition-precipitation (D-P) method.

**Figure captions:**

Fig. 1 Actual Ni loading ( $Ni_A$ ) and yield of Ni loading ( $Y_{Ni}$ ) over Ni/HZSM-5(X) catalysts prepared at various D-P time.

Fig. 2 Conventional FT-IR spectra of HZSM-5 and uncalcined Ni/HZSM-5(X) prepared at various D-P time: (a) HZSM-5; (b) ~ (g), Ni/HZSM-5(X) with D-P time X= 1, 2, 4, 8, 12 and 24 h, respectively.

Fig. 3 Conventional FT-IR spectra of HZSM-5 and calcined Ni/HZSM-5(X) prepared at various D-P time: (a) HZSM-5; (b) ~ (g), Ni/HZSM-5(X) with D-P time X= 1, 2, 4, 8, 12 and 24 h, respectively.

Fig. 4 (i) UV-Vis spectra of HZSM-5; uncalcined 20Ni-HZSM-5(X), X = (b) 2, (c) 4, (d) 12 and (e) 24, respectively; and calcined 20Ni-HZSM-5(X), X = (f) 2, (g) 4, (h) 12, (i) 24, respectively.

Fig. 5  $H_2$ -TPR profiles of Ni/HZSM-5(X) prepared at various D-P time, X = (a) 1 h, (b) 4 h, (c) 12 h, and (d) 24 h.

Fig. 6 XRD patterns of HZSM-5 and Ni/HZSM-5(X) prepared at various D-P time: (a) HZSM-5; (b) ~ (g), Ni/HZSM-5(X) with D-P time X = 1, 2, 4, 8, 12 and 24 h, respectively.

Fig. 7 Change in the dispersion of nickel as a function of D-P time (h).

Fig. 8 N<sub>2</sub> adsorption/desorption isotherms of HZSM-5 and Ni/HZSM-5(X) prepared at various D-P time: (a) HZSM-5; (b) ~ (g), Ni/HZSM-5(X) with D-P time X = 1, 2, 4, 8, 12 and 24 h, respectively.

Fig. 9 FE-SEM images of Ni/HZSM-5(X) prepared at various D-P time; D-P time X = (a) 1 h, (b) 4 h, (c) 12 h, and (d) 24 h.

Fig. 10 O1s and Ni2p XPS spectra for Ni/HZSM-5(X) prepared at various D-P time; D-P time X = (a) 2 h, (b) 4 h, (c) 12 h, and (d) 24 h.

Fig. 11 Vacuum FT-IR spectra over (a) HZSM-5, (b) uncalcined Ni/HZSM-5(4) and (c) Ni/HZSM-5(4) (The specimens are vacuumed for 8 h under 10<sup>-5</sup> Torr at 200 °C).

Fig. 12 Vacuum FT-IR spectra of HZSM-5 and Ni/HZSM-5(X) prepared at different D-P time; (a) HZSM-5; (b) ~ (g), D-P time X = 1, 2, 4, 8, 12 and 24 h, respectively (The specimens are vacuumed for 8 h under  $10^{-5}$  Torr at 400 °C).

Fig. 13 FT-IR spectra for pyridine adsorption over (a) HZSM-5, (b) uncalcined Ni/HZSM-5(4) and (c) calcined Ni/HZSM-5(4).

Fig. 14 FT-IR spectra for pyridine adsorption over HZSM-5 and Ni/HZSM-5(X) prepared at various D-P time; (a) HZSM-5; (b) ~ (e), Ni/HZSM-5(X) with D-P time X= 1, 2, 4, 8 and 24 h, respectively.

Fig. 15  $^{27}\text{Al}$  MAS NMR spectra over Ni/HZSM-5(X) prepared at various D-P time; (a) ~ (d), D-P time X = 1, 4, 12 and 24 h, respectively.

Fig. 16 Proposed mechanisms for the deposition-precipitation (D-P) of Ni(II) species on highly siliceous HZSM-5 zeolite.

Figure 1

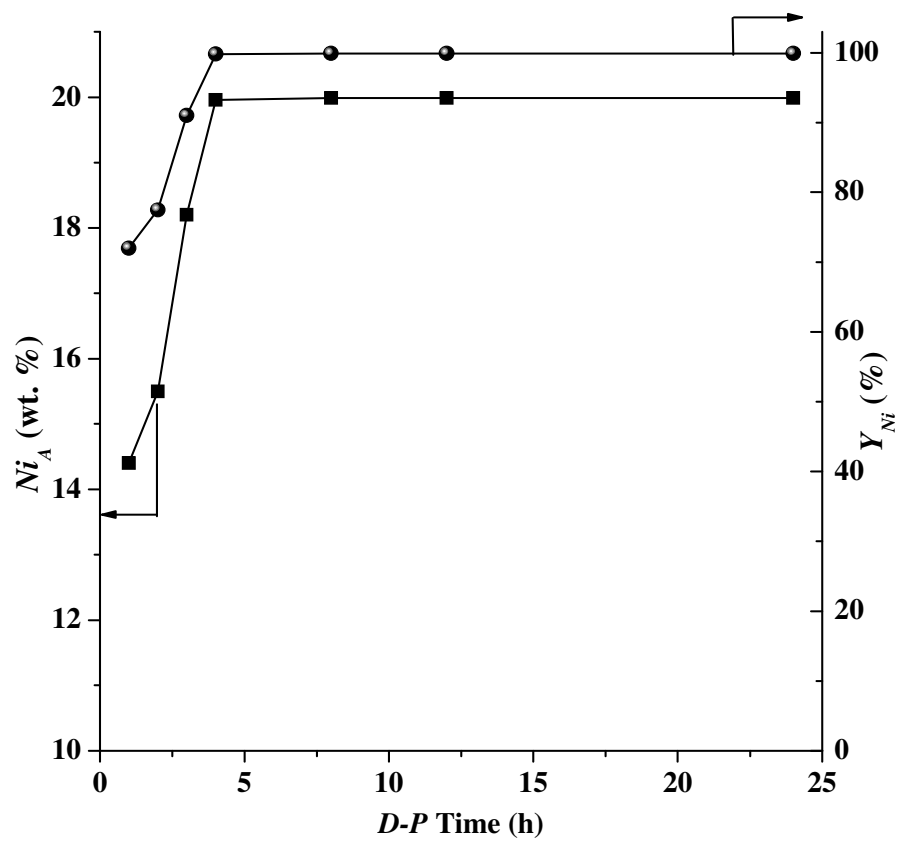


Fig. 1 Actual Ni loading ( $Ni_A$ ) and yield of Ni loading ( $Y_{Ni}$ ) over Ni/HZSM-5(X) catalysts prepared at various D-P time.

Figure 2

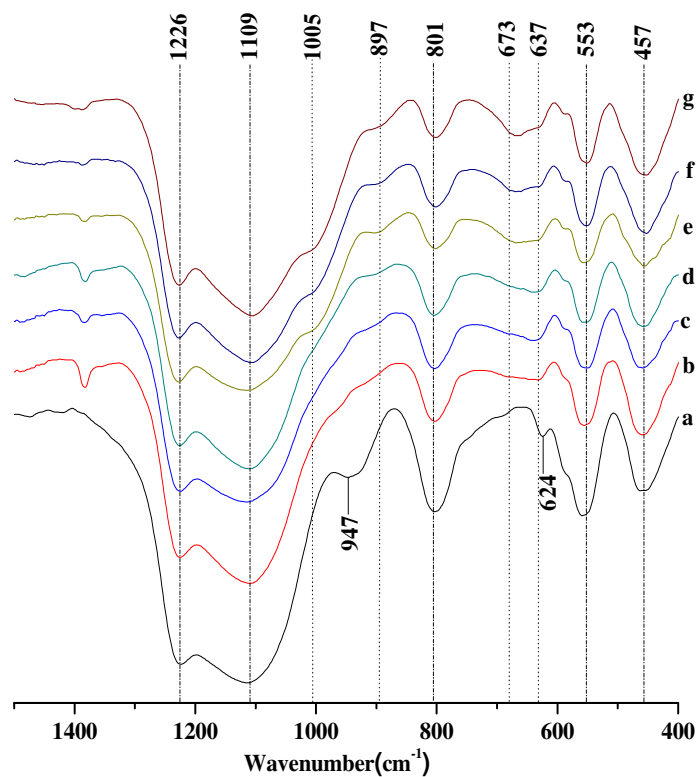


Fig. 2 Conventional FT-IR spectra of HZSM-5 and uncalcined Ni/HZSM-5(X) prepared at various D-P time: (a) HZSM-5; (b) ~ (g), Ni/HZSM-5(X) with D-P time X= 1, 2, 4, 8, 12 and 24 h, respectively.

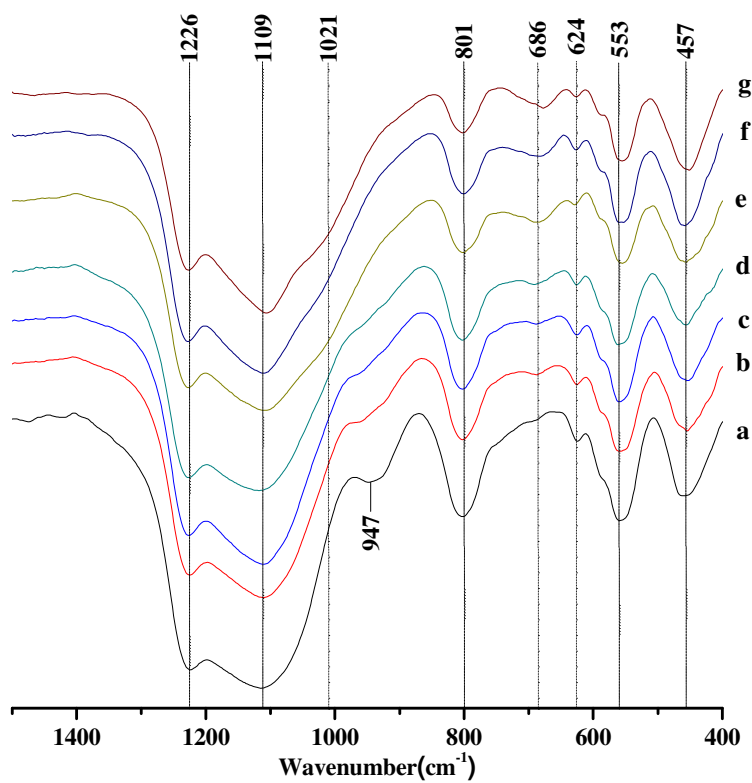
**Figure 3**

Fig. 3 Conventional FT-IR spectra of HZSM-5 and calcined Ni/HZSM-5(X) prepared at various D-P time: (a) HZSM-5; (b) ~ (g), Ni/HZSM-5(X) with D-P time X= 1, 2, 4, 8, 12 and 24 h, respectively.

Figure 4

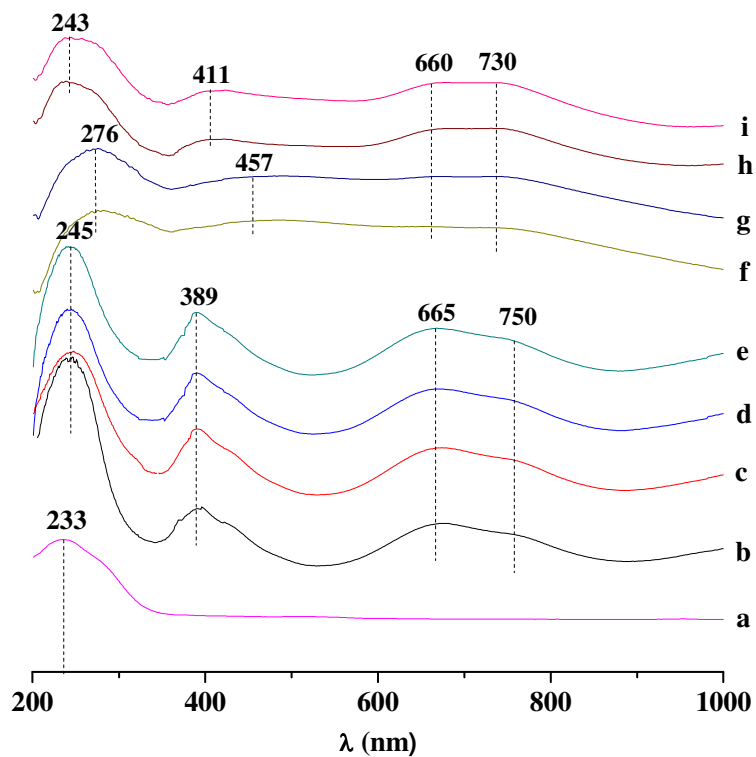


Fig. 4 (i) UV-Vis spectra of HZSM-5; uncalcined 20Ni-HZSM-5(X), X = (b) 2, (c) 4, (d) 12 and (e) 24, respectively; and calcined 20Ni-HZSM-5(X), X = (f) 2, (g) 4, (h) 12, (i) 24, respectively.

Figure 5

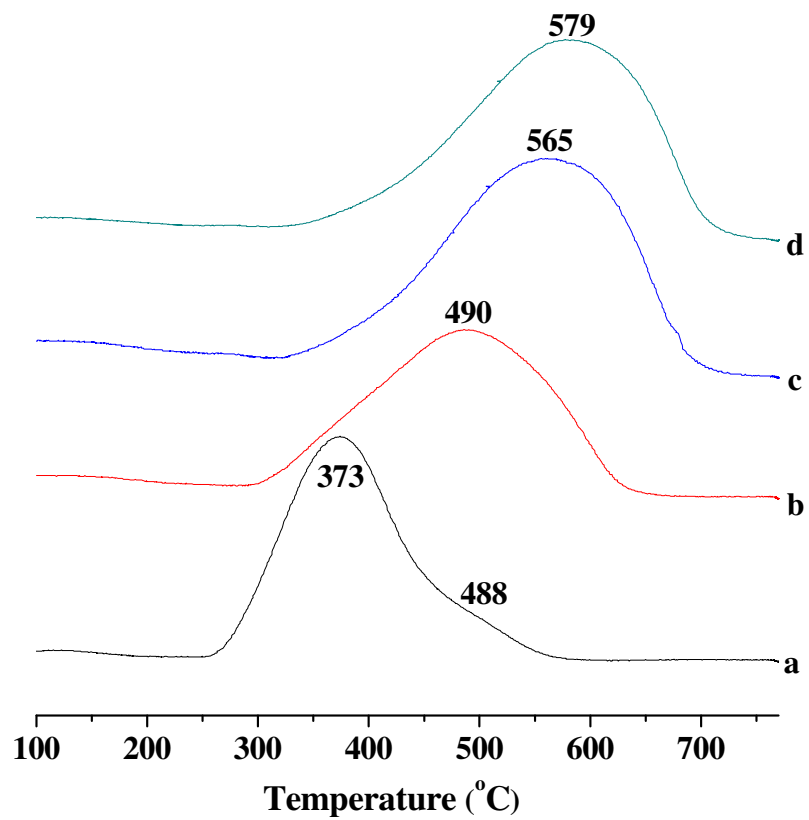


Fig. 5 H<sub>2</sub>-TPR profiles of Ni/HZSM-5(X) prepared at various D-P time, X =

(a) 1 h, (b) 4 h, (c) 12 h, and (d) 24 h.

Figure 6

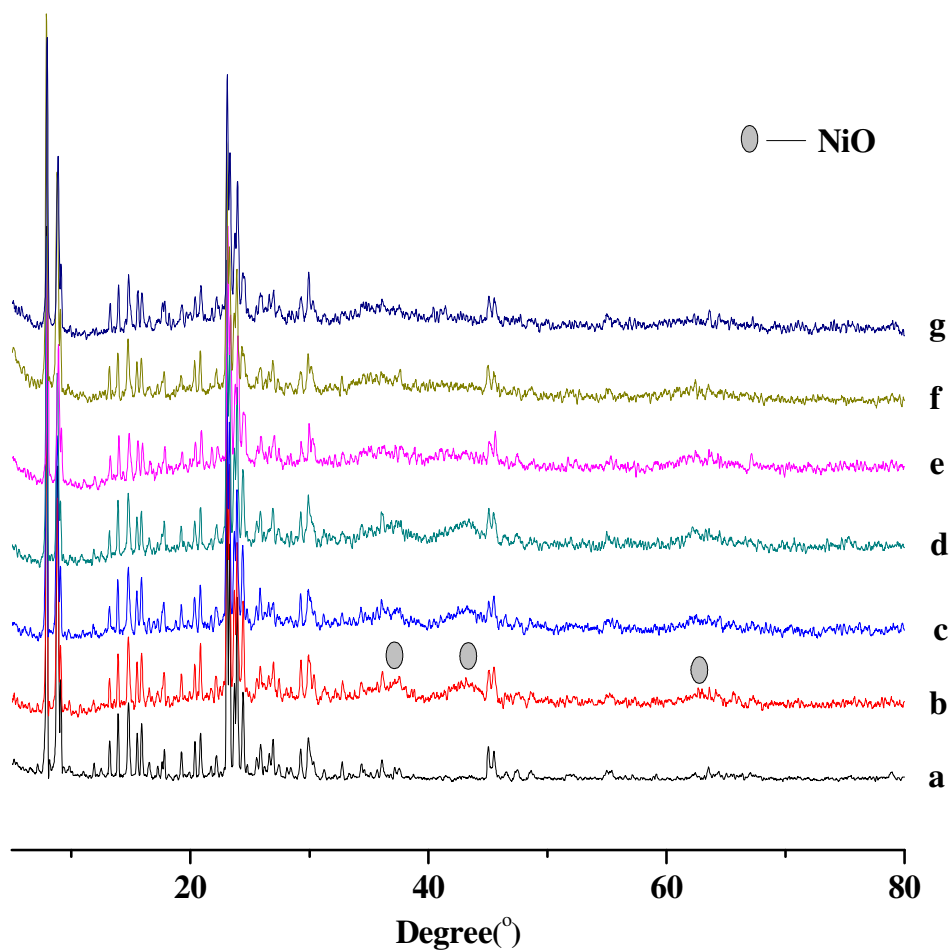


Fig. 6 XRD patterns of HZSM-5 and Ni/HZSM-5(X) prepared at various D-P time: (a) HZSM-5; (b) ~ (g), Ni/HZSM-5(X) with D-P time X = 1, 2, 4, 8, 12 and 24 h, respectively.

Figure 7

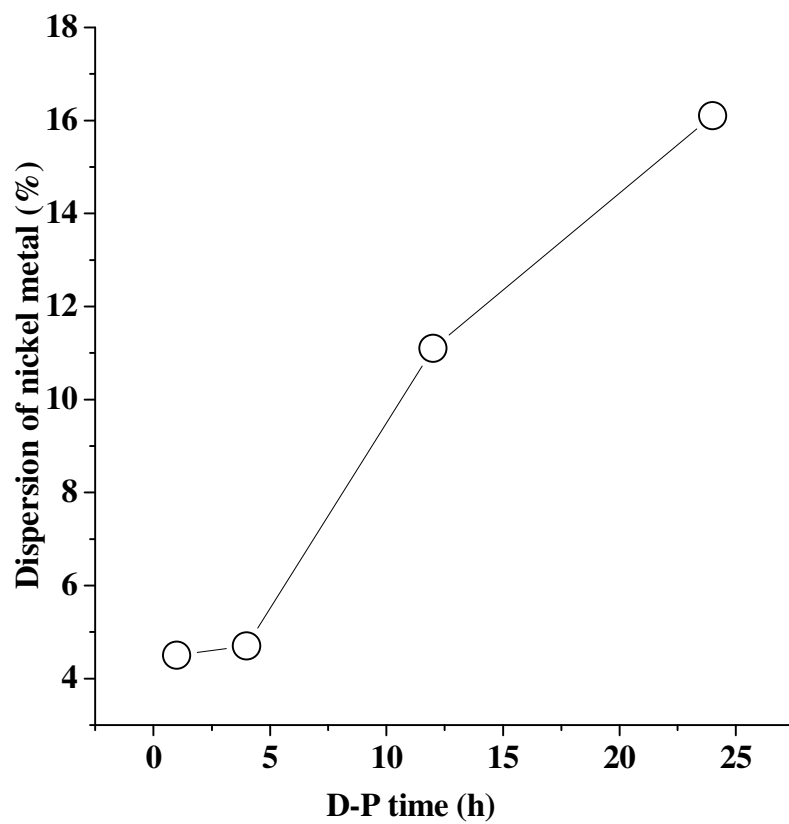


Fig. 7 Change in the dispersion of nickel as a function of D-P time (h).

Figure 8

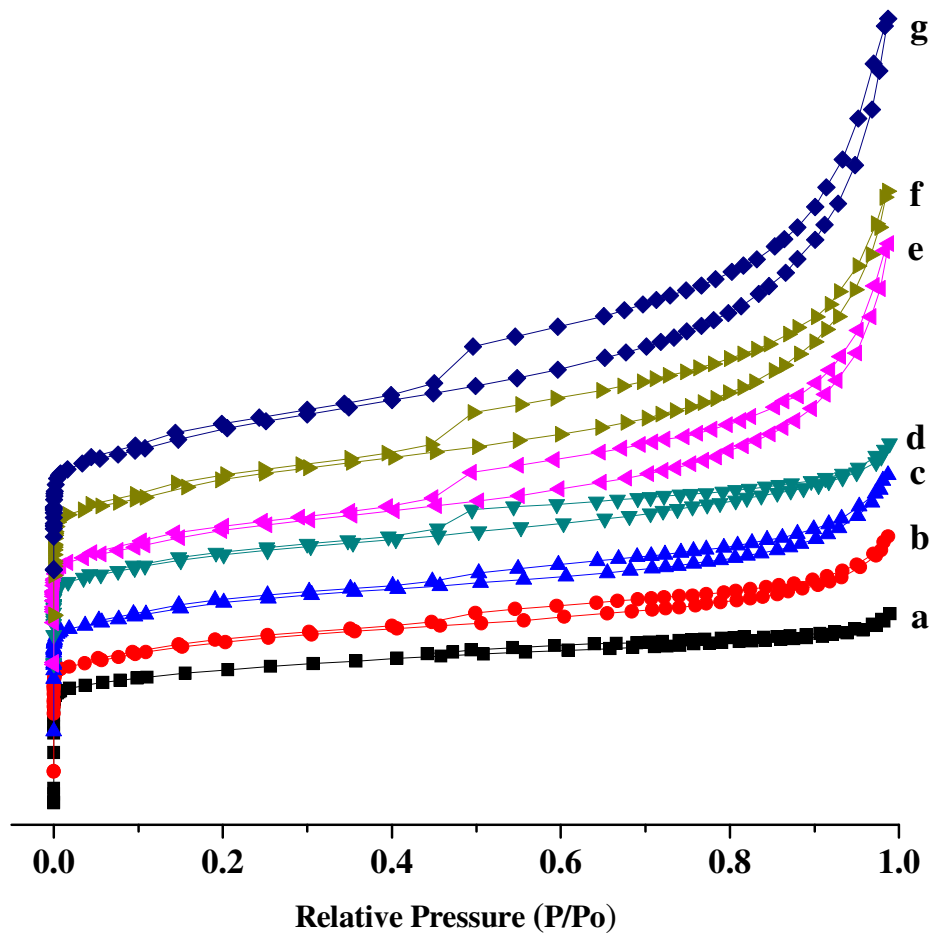


Fig. 8  $N_2$  adsorption/desorption isotherms of HZSM-5 and Ni/HZSM-5(X) prepared at various D-P time: (a) HZSM-5; (b) ~ (g), Ni/HZSM-5(X) with D-P time  $X = 1, 2, 4, 8, 12$  and  $24$  h, respectively.

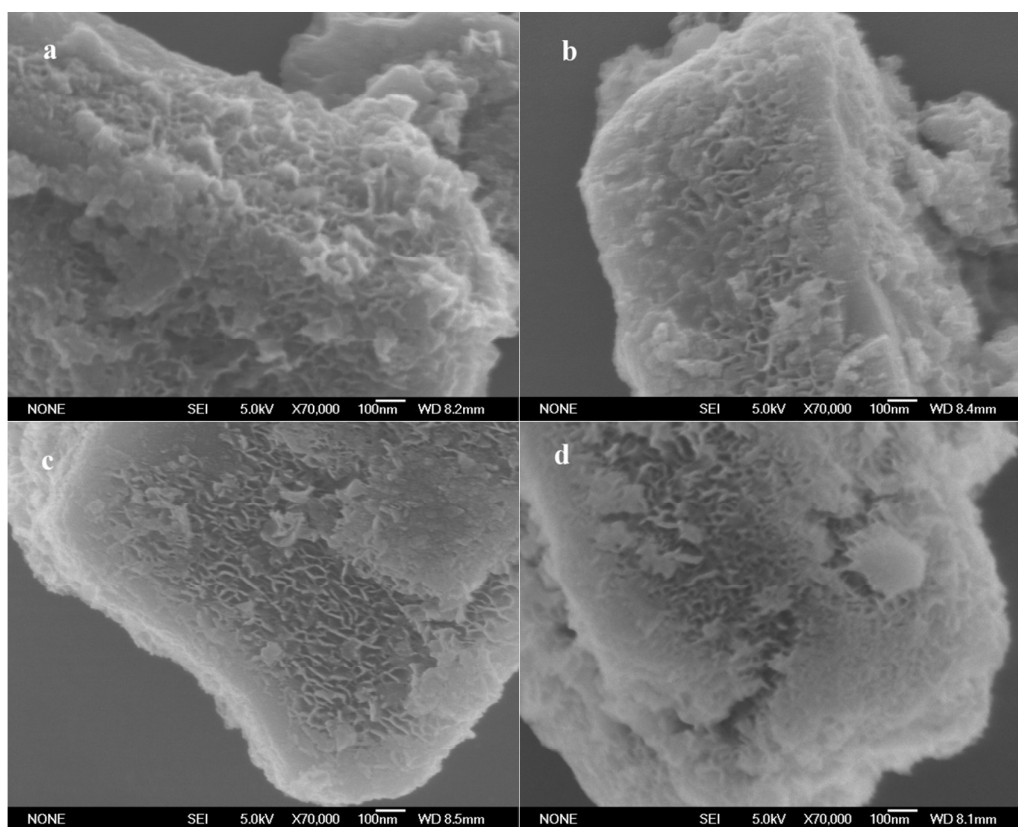
**Figure 9**

Fig. 9 FE-SEM images of Ni/HZSM-5(X) prepared at various D-P time; D-P time X = (a) 1 h, (b) 4 h, (c) 12 h, and (d) 24 h.

Figure 10

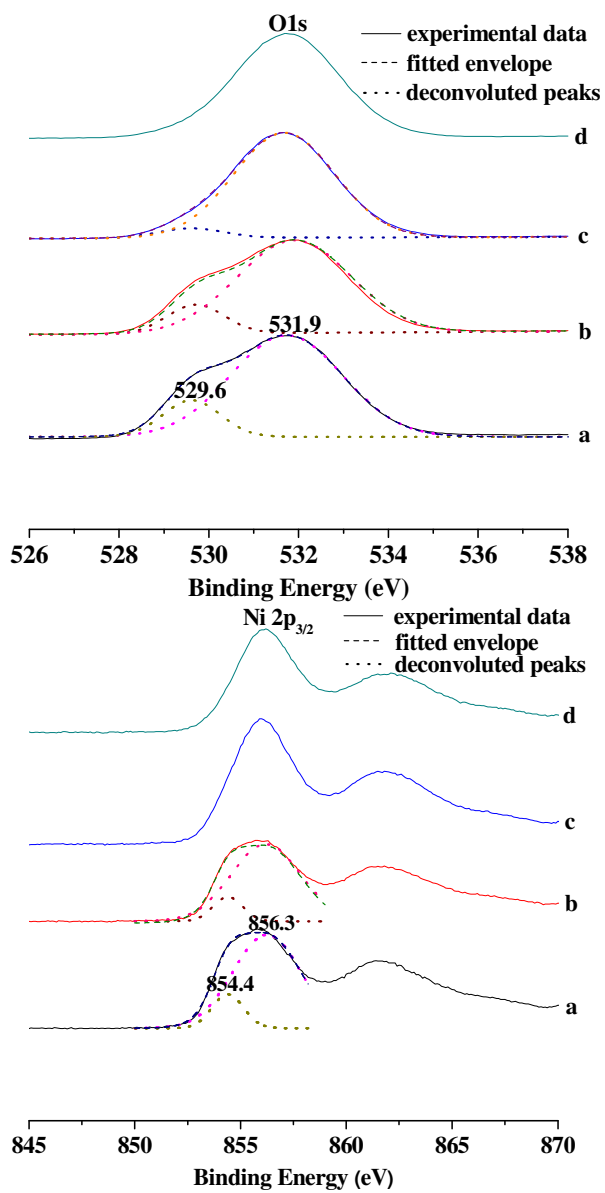


Fig. 10 O1s and Ni2p XPS spectra for Ni/HZSM-5(X) prepared at various D-P time; D-P time X = (a) 2 h, (b) 4 h, (c) 12 h, and (d) 24 h.

Figure 11

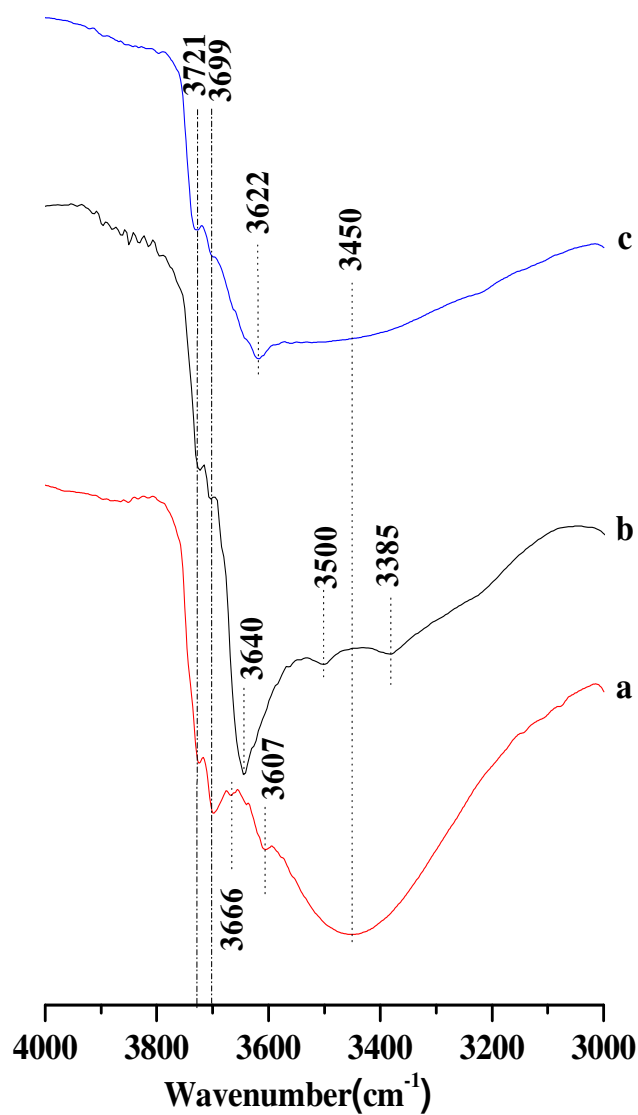


Fig. 11 Vacuum FT-IR spectra over (a) HZSM-5, (b) uncalcined Ni/HZSM-5(4) and (c) Ni/HZSM-5(4) (The specimens are vacuumed for 8 h under  $10^{-5}$  Torr at 200 °C).

Figure 12

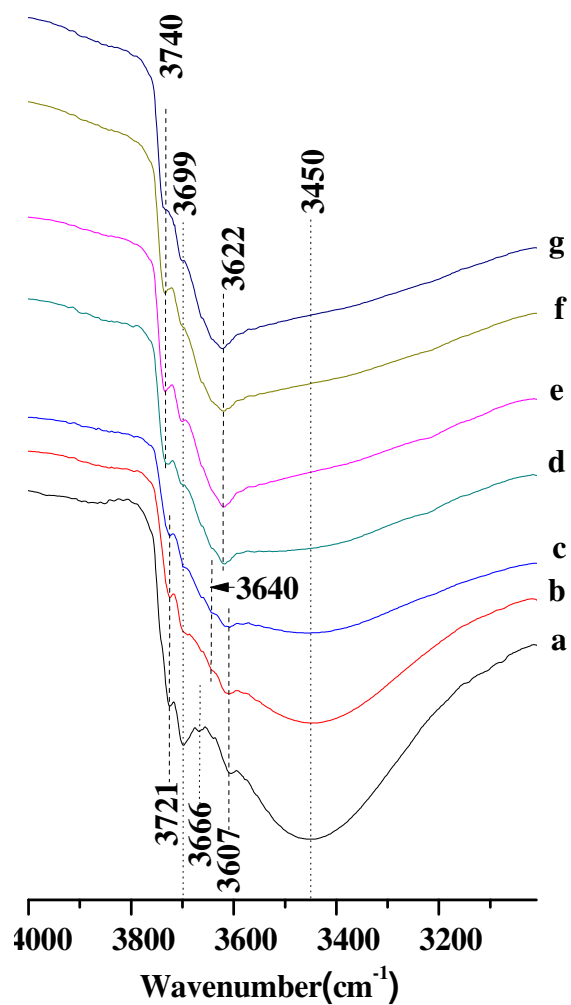


Fig. 12 Vacuum FT-IR spectra of HZSM-5 and Ni/HZSM-5(X) prepared at different D-P time; (a) HZSM-5; (b) ~ (g), D-P time X = 1, 2, 4, 8, 12 and 24 h, respectively (The specimens are vacuumed for 8 h under  $10^{-5}$  Torr at 400 °C).

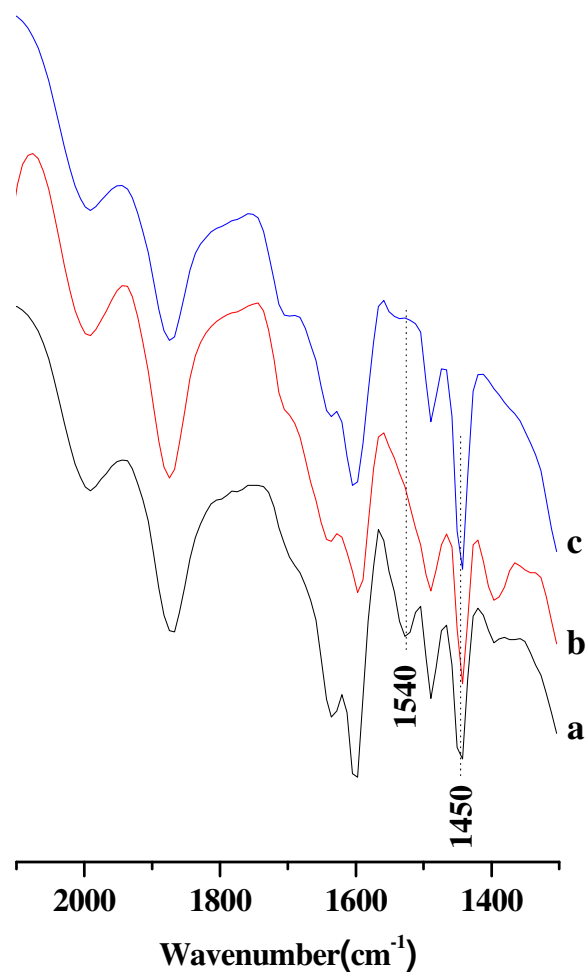
**Figure 13**

Fig. 13 FT-IR spectra for pyridine adsorption over (a) HZSM-5, (b) uncalcined Ni/HZSM-5(4) and (c) calcined Ni/HZSM-5(4).

Figure 14

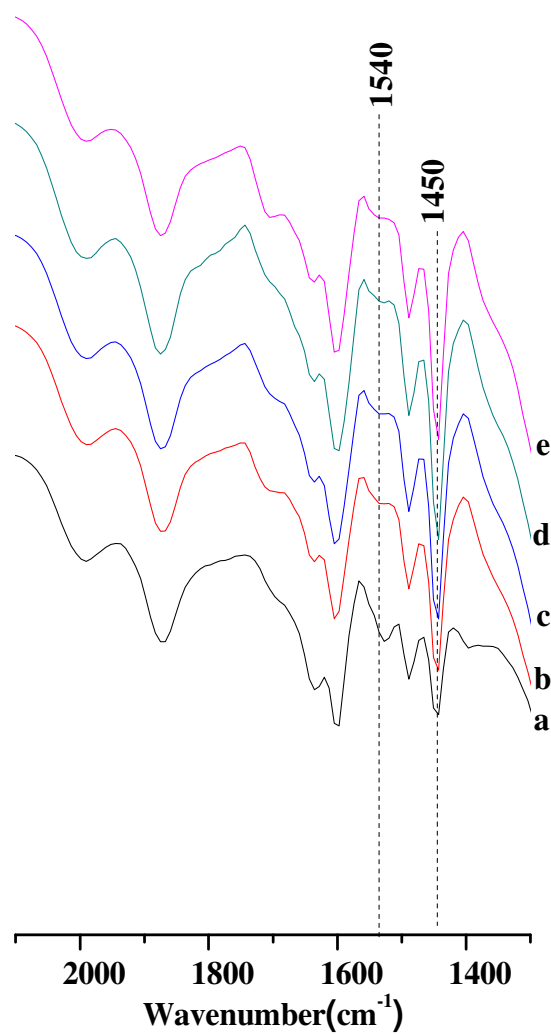


Fig. 14 FT-IR spectra for pyridine adsorption over HZSM-5 and Ni/HZSM-5(X) prepared at various D-P time; (a) HZSM-5; (b) ~ (e), Ni/HZSM-5(X) with D-P time X= 1, 2, 4, 8 and 24 h, respectively.

Figure 15

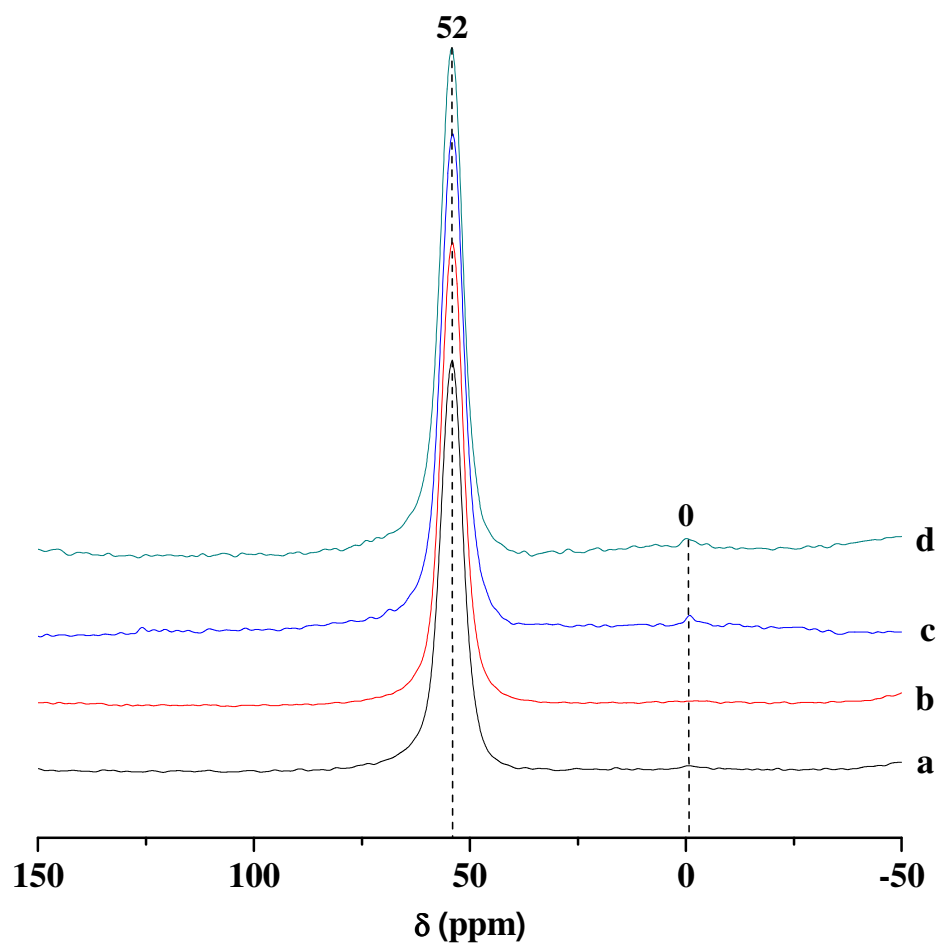


Fig. 15  $^{27}\text{Al}$  MAS NMR spectra over Ni/HZSM-5(X) prepared at various D-P time; (a) ~ (d), D-P time X = 1, 4, 12 and 24 h, respectively.

Figure 16

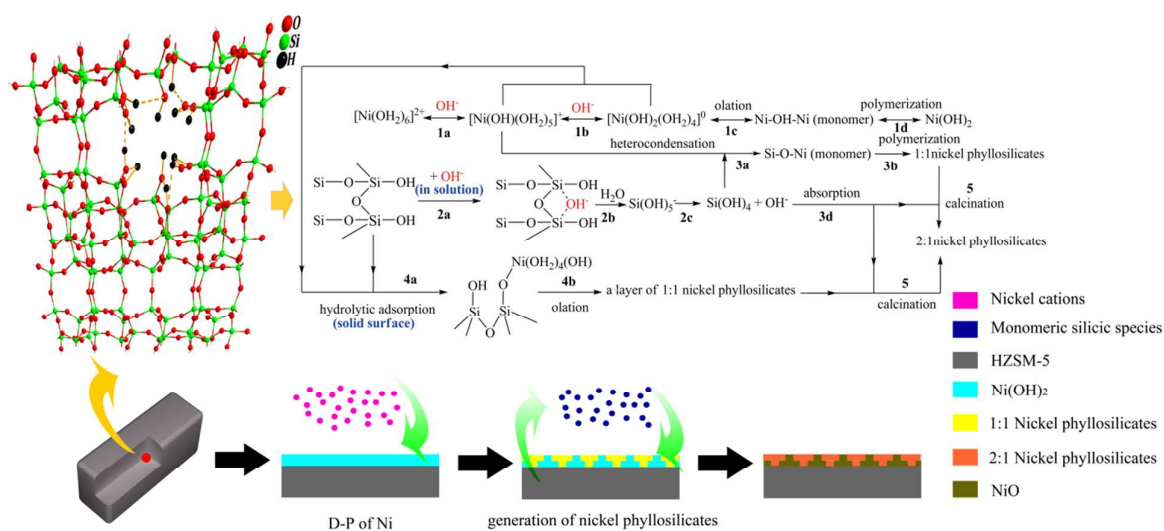


Fig. 16 Proposed mechanisms for the deposition-precipitation (D-P) of Ni(II) species on highly siliceous HZSM-5 zeolite